

GSA Data Repository 2015320

Regional Setting

The Northwest African continental margin (see review in Lünig et al., 2004) and shelf in particular were major sites of strongly enhanced organic carbon burial during OAE2 (Kuhnt et al., 2001; Kuypers et al., 2002; Kolonic et al., 2005). The Tarfaya Basin on the NW African Shelf contains more than 500 m of Upper Cretaceous laminated OC-rich biogenic sediments (Leine, 1986), deposited with high sedimentation rates (Kuhnt et al., 2001; Meyers et al., 2012), allowing investigation of paleoceanographic changes and climatic events at centennial time-scale resolution (Kuhnt et al. 2001, 2005). High-resolution inorganic, organic, and isotopic geochemical records from a depth transect through the mid-Cretaceous shelf basin (Kolonic et al, 2002, 2005) revealed high-amplitude fluctuations in the accumulation of oil-prone (kerogen Type II) organic carbon, redox-sensitive and sulfide-forming trace metals, and biomarkers indicative of photic zone euxinia. These fluctuations in general occurred synchronous across the basin, suggesting a close link between climate variability, carbon burial and redox conditions. The pacing and regularity of the records has been interpreted to represent a dynamic depositional setting controlled by orbital and higher frequency forcing (Kolonic et al., 2005; Meyers et al., 2012), consistent with other high resolution records from the central North and South Atlantic basins (Wagner et al., 2013). Cases have been made for all main orbital bands (short eccentricity, obliquity, precession) and sub-orbital variations (Kuhnt et al. 1997; Kuhnt et al 1994; Kolonic et al., 2005; Kuhnt et al., 2001; Kuhnt et al. 2003; Meyers et al., 2012). However, no final conclusion has yet been reached on the dominant frequency, but obliquity has been favoured in many studies, including the most recent analyses by Meyers et al. (2012), with eccentricity forcing possibly also being a secondary component in parts of the record.

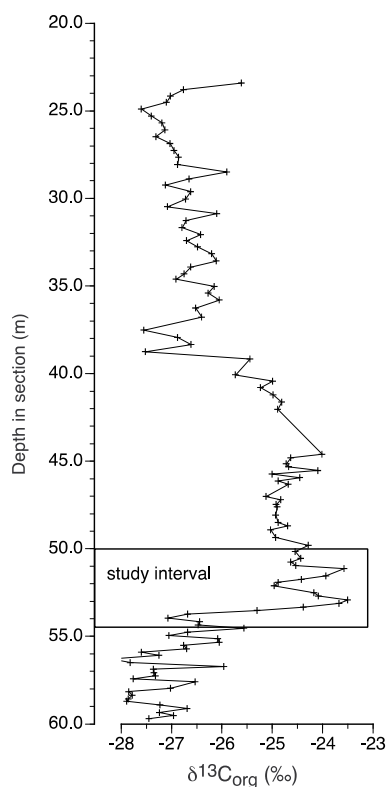


Figure DR1. C_{org} isotope profile through core S57 from Kolonic et al. (2005), showing the interval analysed in this study.

Methods

Samples for this study were taken from core S57, spanning an interval of about 4.3 m that starts ~60 cm before the onset of the C isotope excursion in this region and covers the initial maximum extent of the excursion (Figure DR1). Samples were dried and ground in an agate mortar before total (TC) and organic carbon (TOC) contents were measured using a LECO CS-300 carbon-sulfur analyzer (with a RSD of $\pm 3\%$). For TOC determinations, inorganic carbon was carefully removed by repetitive addition of 0.25 N HCl. $\delta^{13}\text{C}$ values (RSD = $\pm 0.1\%$) are reported relative to Vienna Pee Dee belemnite (VPDB) and were measured on decalcified sediments, using automated on-line combustion followed by conventional isotope-ratio mass spectrometry.

Iron speciation (Table DR1) was determined via the sequential extraction technique of Poulton and Canfield (2005). This method extracts different operationally-defined Fe pools, including Fe carbonates such as siderite (Fe_{carb}), ferric oxides such as goethite and hematite (Fe_{ox}), and magnetite (Fe_{mag}). These minerals define an iron pool which is considered 'highly reactive' (Fe_{HR}) during sedimentation and diagenesis (Raiswell and Canfield, 1998). Pyrite (Fe_{py}) was determined via the standard chromous chloride distillation technique, while acid volatile sulfides (Fe_{AVS}) were determined via a hot 6 M HCl extraction (Canfield et al., 1986). In all cases, Fe_{AVS} was only a minor phase as expected in sediments of this age (Table DR1). Fe_{AVS} is generally effectively solubilised during the first phase of the sequential Fe procedure (i.e. during the step to extract Fe_{carb} ; Poulton and Canfield, 2005), and thus Fe_{HR} is calculated as $\text{Fe}_{\text{carb}} + \text{Fe}_{\text{ox}} + \text{Fe}_{\text{mag}} + \text{Fe}_{\text{py}}$. All Fe solutions were measured via AAS. Due to the calcareous nature of these shales, all extractions were scaled up in order to increase the sensitivity and reproducibility of the extractions, as previously performed on similar lithology OAE sediments from the proto-North Atlantic (März et al., 2008). In support of this approach, replicate extractions gave a RSD of $<5\%$ for all techniques.

Recently, Clarkson et al. (2014) demonstrated the utility of carbonate-rich lithologies for determining water column redox conditions via Fe speciation. This study demonstrated that carbonates such as limestones and dolomites provide a robust indication of water column redox conditions when total Fe is greater than 0.5 wt%, as long as the samples have not been affected by Fe addition during deep burial dolomitization. However, Clarkson et al. (2014) also highlight that caveats exist with regard to this FeT threshold, particularly with organic-rich calcareous shales such as those of the present study, whereby Fe speciation may still provide robust results at much lower total Fe. For rocks of this nature, Clarkson et al. (2014) suggest that total Fe contents should be considered on an organic C-free basis, with the utility of the data evaluated within the context of each particular study. Our Tarfaya samples have an average FeT of 0.88 ± 1.67 wt% (0.67 ± 0.58 wt% when 5 samples with anomalously high FeT are discounted) when considered on a CH_2O -free basis, with ~50% of the samples containing >0.5 wt% FeT. Furthermore, as shown in Figure DR2, there is no relationship between FeT content and the redox cyclicity, and instead, with the exception of a few outliers with anomalously high FeT (which arises due to unusually low CaCO_3 and/or high pyrite Fe for these samples), FeT content is controlled by CaCO_3 content; Figure DR3). This suggests that our identification of repetitive ferruginous intervals is not a consequence of a bias introduced by low FeT contents across these intervals. We conclude, therefore, that our Fe speciation data provide a robust indication of water column redox conditions, despite dilution of FeT by high CaCO_3 , consistent with detailed studies of other anoxic calcareous shales from Phanerozoic settings (e.g., Raiswell et al., 2001).

Pyrite S isotope compositions were determined via EA-IRMS on Ag_2S precipitates from the chromous chloride extractions. Carbonate associate sulfate (CAS) was determined on 10-20 g of homogenized sediment according to recently refined techniques (Goldberg et al., 2011). Carbonate in these shales consists dominantly of calcareous nannoplankton and planktonic forams, and the specific samples chosen for CAS analyses ranged in CaCO_3 from 56-96 wt%, making them ideal for this technique. Samples were washed twice with 10% v/v NaCl to remove soluble sulfate,

followed by three washes with 5% NaOCl to remove sulfide and organic S. Samples were then washed an additional three times with 10% v/v NaCl, until no BaSO₄ precipitate was observed upon addition of BaCl₂ to the filtrate. Carbonate associated sulfate was then dissolved by addition of 10% HCl to the sediment, and after centrifugation the pH of the extractant was adjusted to 2-3 and BaSO₄ was precipitated by the addition of BaCl₂. We did not remove Fe (oxyhydr)oxides prior to addition of the BaCl₂, as the combustion technique used for sulfur isotope analysis is not affected by the presence of Fe minerals. This circumvents the possibility for sulfate removal from the extract through adsorption to Fe (oxyhydr)oxides, but has the disadvantage that sulfate concentrations could not be determined. All sulfur isotope compositions (Table DR1) are reported with respect to VCDT.

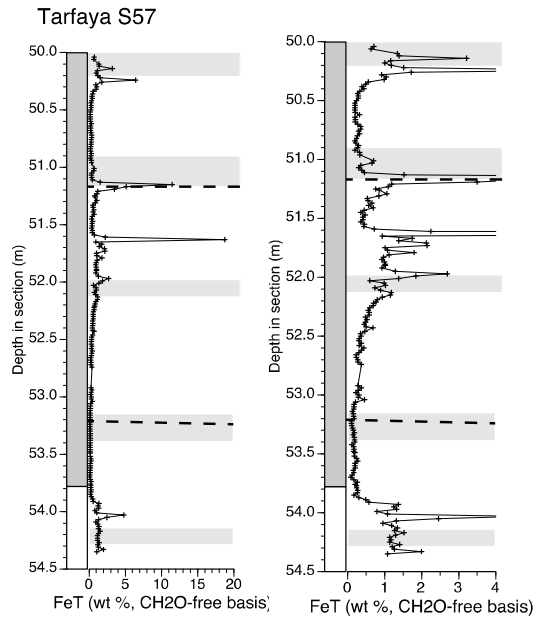


Figure DR2. Plots showing FeT on an organic matter-free basis (assuming a simple formula of CH₂O). Left pane shows the entire data-set, right pane focusses on the majority of the data with FeT between 0-4 wt%.

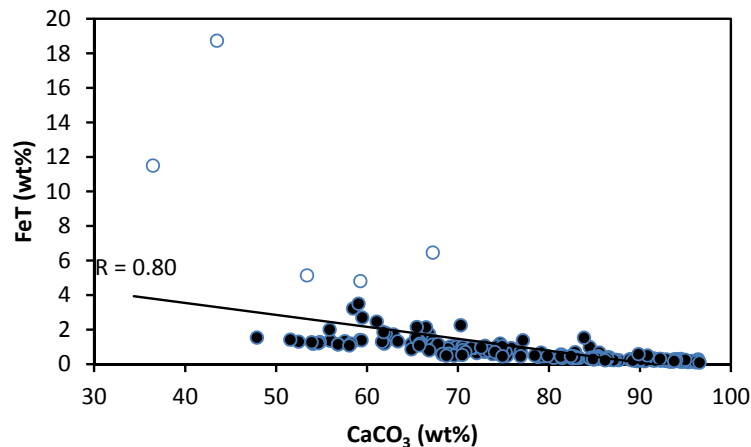


Figure DR3. Total Fe as a function of CaCO₃. The R value is calculated discounting the five samples with anomalously high FeT (open circles).

It has been demonstrated that the S isotopic composition of CAS can accurately record the sulfate isotopic composition of seawater (Burdett et al., 1989; Strauss, 1999; Gill et al., 2008). Nevertheless, before interpretation of the CAS isotopic record, it is important to test the fidelity of the record, since post-depositional processes (such as authigenic carbonate formation during early diagenesis) and post-sampling processes (such as pyrite oxidation during storage or CAS extraction) may potentially bias the record. Pyrite concentrations were low throughout our CAS samples (0.29 ± 0.19 wt%), with no relationship evident between pyrite concentration and CAS $\delta^{34}\text{S}$ (Figure DR4). Similarly, we found no relationship between the CAS and pyrite S isotopic measurements (Figure DR4). Furthermore, as highlighted by Adams et al. (2010), incorporation of porewater sulfate during authigenic carbonate formation should result in a ^{32}S -enriched sulfate signal as a result of initial depletion of porewater ^{32}S during bacterial sulfate reduction. However, our CAS sulfur isotopic values are significantly lighter than values measured from other contemporaneous marine basins at this time (e.g., Ohkouchi et al., 1999; Paytan et al., 2004), suggesting that sulfate uptake via authigenic carbonate formation in these calcareous pelagic microfossil-rich samples was not a prevalent process. It should also be noted, however, that our values for the onset of OAE2 at Tarfaya ($10 \pm 2\text{‰}$) are similar to those determined during the run-up to OAE2 in the Western Interior Seaway (10-13‰) (Adams et al., 2010), which provides further support for the integrity of our data. Together, these observations suggest that our pre-treatment stages to remove soluble sulfate and pyrite (see above) were effective at preventing significant contamination of the seawater CAS isotopic record (see also Adams et al., 2010).

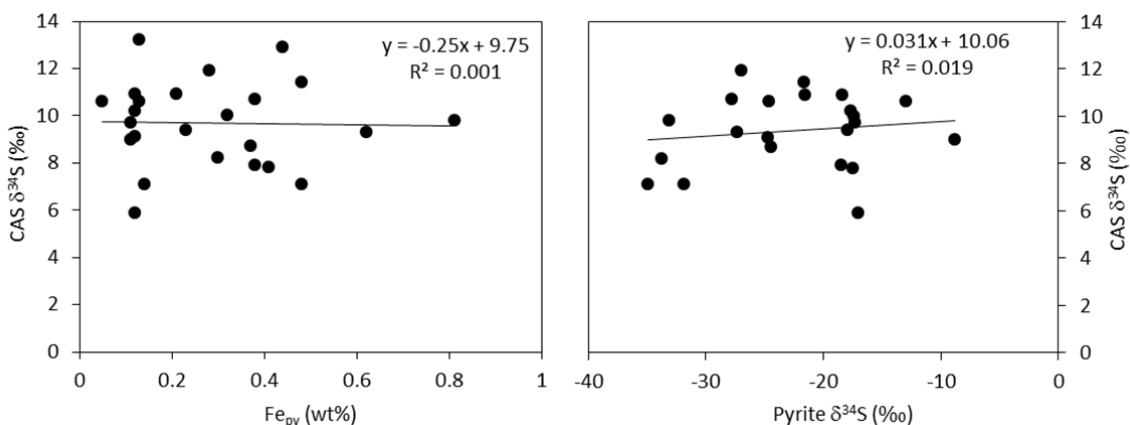


Figure DR4. Plots of CAS $\delta^{34}\text{S}$ as a function of pyrite concentration and pyrite $\delta^{34}\text{S}$.

For biomarker analyses, ground and homogenized sediment samples (~5 g) were extracted with an accelerated solvent extractor (ASE) with DCM:MeOH (9:1) at the Royal Netherlands Institute for Sea Research (NIOZ). The total extracts were dried under N_2 in a rotary evaporator, dissolved in a minimum volume of DCM and consequently absorbed on activated Al_2O_3 . The alumina (with the absorbed extract) was dried and transferred on a large column with activated Al_2O_3 for subsequent chromatographic separation of the apolar and polar fractions. The apolar fraction was obtained by elution with n-hexane/DCM (9:1 v:v), the polar fraction by elution with DCM/methanol (1:1 v:v). The fractions were collected in round-bottom flasks, evaporated, transferred into pre-weighed vials, dried under N_2 , and weighed again. The apolar fraction was stored in hexane. Desulfurization of the polar fraction was performed with the Raney-nickel method described by Petit and Van Tamelen (1962) and Sinninghe Damsté et al. (1990) to liberate sulfur-bond biomarkers. Before desulfurization, a standard (D2-C22 thiophene) was added to the

extract. The desulfurized polar fraction was again separated into polar and apolar fraction by small column separation with activated Al_2O_3 and the obtained apolar fraction was hydrogenated by addition of 3 ml of EtOAc, a drop of concentrated acetic acid, and platinum oxide. The vials were flushed with H_2 for 1 h and stirred overnight, and biomarkers including isorenieratane were identified and quantified by gas chromatography (GC) and gas chromatography-mass spectrometry (GC-MS).

For major elements determination (Al, Ba, Ca, Fe, K, Mg, Mn, Na, P, S, Sr, und Ti), about 50 mg of sample was digested in a mixture of 3 ml HNO_3 (65%), 2 ml HF (40%) and 2 ml HCl (36%) of supra-pure quality at 200°C and 30 kbar in closed Teflon vessels (Heinrichs et al., 1986). After drying by evaporation, the residue was re-dissolved with 0.5 ml HNO_3 (65%) and 4.5 ml deionised water. Subsequently, the solutions were analysed with ICP-AES, and the results checked with international standard reference material; relative standard deviations were below 3%. The Site 1261 Si data were determined by wavelength-dispersive XRF on glass beads prepared from freeze-dried sediments (for details, see März et al., 2010). The K/Si ratio is based on the K and Si fractions in excess of the minimum lithogenic background (calculated after Brumsack, 2006).

The morphology of pyrite and Fe oxide minerals was examined via scanning electron microscopy (SEM) in both backscatter and secondary electron mode. These analyses were augmented by chemical analyses using energy dispersive x-ray spectroscopy (EDS).

Results

Evaluation of sulfide oxidation

Kraal et al. (2009) demonstrate significant oxidation of pyrite in sediment cores that were exposed to oxygen and stored undried at 4°C for a number of years. This pyrite oxidation generated acidity that resulted in transformation of P in authigenic Ca-P minerals to Fe oxide-bound P in carbonate poor samples. In contrast, significant P transformation after sampling did not occur in sediments containing appreciable carbonate (>5 wt% CaCO_3), which is much lower than the carbonate content of our samples (Table DR1).

In addition to ruling out significant post-recovery mobilization of P due to the high carbonate contents, there are a number of reasons to consider that pyrite oxidation has not altered our redox interpretation for samples from core S57. First, core S57 has been stored dry in a core facility under ambient conditions since recovery, which greatly diminishes rates of pyrite oxidation. This is consistent with the lack of any visible surface oxidation that would be documented by gypsum, elemental sulfur, or Fe oxide precipitation. Second, our samples still contain Fe_{AVS} (Table DR1) in the form of iron monosulfides such as mackinawite, which are extremely reactive towards oxygen and hence their persistence rules out significant oxidation of Fe sulfide minerals, which in sediments of this age dominantly comprise more stable pyrite. In support of this, the product of Fe sulfide oxidation, Fe_{ox} , is low throughout the euxinic intervals in comparison to Fe_{carb} and Fe_{py} , and even with some pyrite oxidation, our interpretation of euxinia would still be robust, as Fe sulfide oxidation would only decrease the euxinic signal. Furthermore, given the lack of any distinct or repetitive change in lithology across ferruginous intervals, there is no apparent reason why ferruginous intervals occurring on orbital timescales would be an artefact of preferential Fe sulfide oxidation. Finally, a lack of significant pyrite oxidation is conclusively demonstrated by SEM analyses. Figure DR5 shows a range of representative morphologies and accompanying EDS spectra for samples from euxinic and ferruginous horizons. Pyrite framboids with a small and limited size-range are abundant in euxinic samples (Figures DR5A, DRB). These framboids show no evidence for oxidation, with EDS spectra suggesting Fe sulfide framboids with minor background CaCO_3 and silicate. Ferruginous samples (Figures DR5C-DRF) also contain framboids, which tend to be more variable in size (e.g., Figure DR5C), consistent with a diagenetic origin (e.g., Wignall and Newton, 1998) (note that we did not attempt any statistical

analysis of the range of framboid diameters, as this technique has never been calibrated for anoxic ferruginous conditions). Importantly, EDS spectra for the framboids in ferruginous samples show no evidence for oxidation. Furthermore, Figure DR5F shows a mineral aggregate, with a larger hexagonal pyrite crystal (showing no evidence for oxidation) surrounded by partially sulfidized Fe oxide minerals. This Fe oxide aggregate is entirely consistent with the form of Fe oxides formed at the chemocline under ferruginous water column conditions (Zegeye et al., 2012), rather than being consistent with detrital Fe oxides (Poulton and Raiswell, 2005), and provides strong support for the delivery of water column Fe oxide precipitates to the sediment under ferruginous conditions, followed by partial sulfidation during early diagenesis. Such aggregates were not observed in euxinic samples, consistent with the delivery of water column Fe to the sediment via the formation of small pyrite framboids. Taken together, these mineralogical observations and chemical analyses conclusively rule out significant oxidation of Fe sulfide minerals in core S57, providing support for the robust nature of our redox interpretations.

Ferruginous vs euxinic intervals

As discussed in the main text, redox cyclicity is not controlled by changes in lithology (in terms of carbonate or TOC variability). Figure DR6 shows this lack of lithological variability across a prominent ferruginous interval, and also shows that ferruginous intervals are not related to repetitive variability in CaCO₃ or TOC contents.

Nutrient availability

Nutrient limitation is one mechanism that could potentially restrict primary productivity and the formation of the organic matter required to fuel bacterial sulfate reduction, hence limiting sulfide production and the persistence of euxinia. However, organic matter contents are high throughout the studied section and show no systematic variation with the redox cyclicity (Figure DR6), suggesting that productivity and organic carbon burial were not affected by perturbations to the P or N cycles on orbital timescales. An alternative, more direct influence on sulfate reduction rates may have been through drawdown of bio-essential trace metals from the water column under euxinic conditions. Iron, zinc and cobalt are the only bioactive metals known to be essential to the microbial sulfate reduction pathway (Fraústo da Silva and Williams, 2001). The concentrations of Co and Zn (normalized to Al) are shown in Figure DR7. The lack of any systematic trends between ferruginous and euxinic intervals, coupled with the fact that both elements are enriched relative to average shale, suggests that the availability of these elements was unlikely to have limited bacterial sulfate reduction during OAE2.

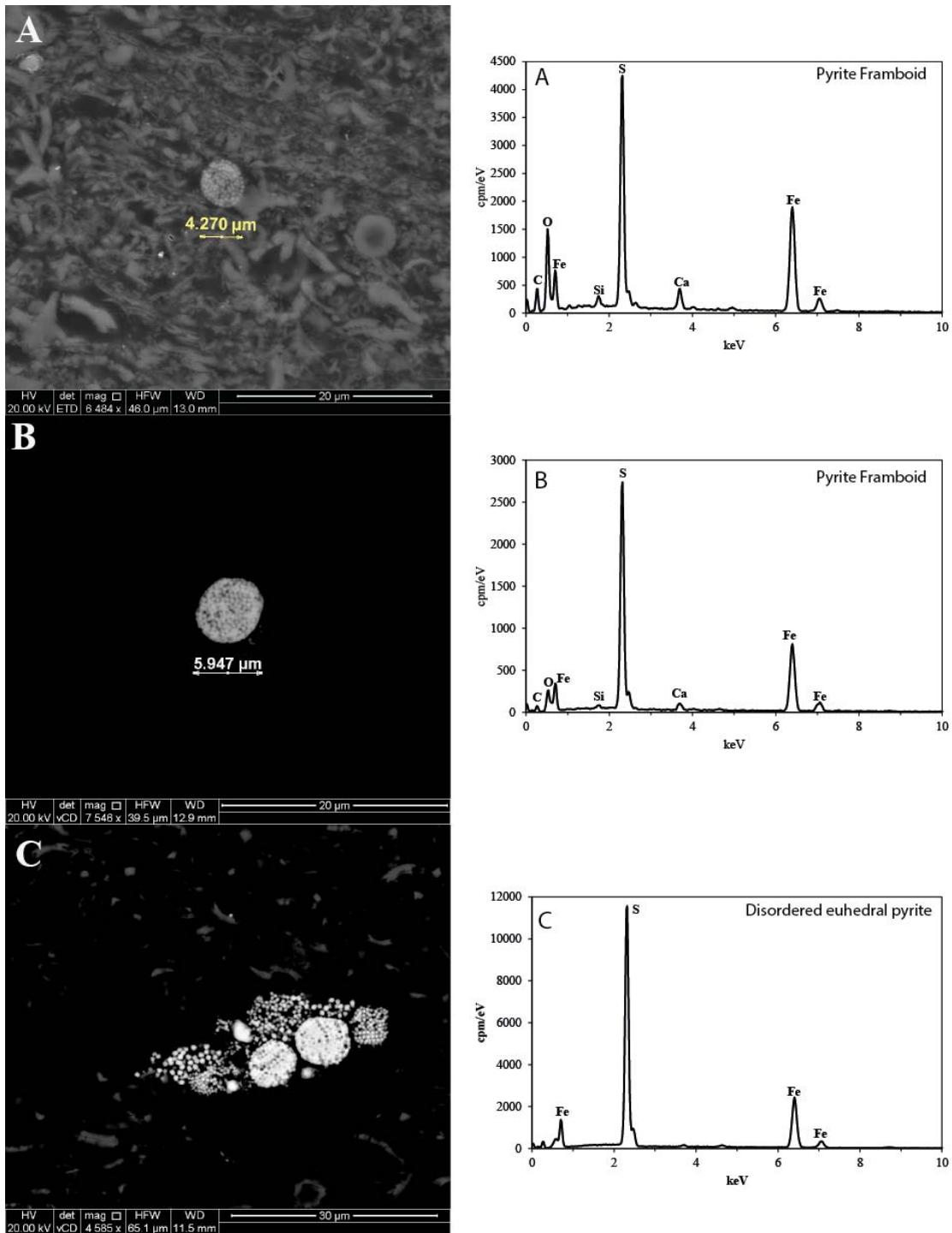


Figure DR5. SEM images of representative Fe minerals from euxinic and ferruginous intervals, and accompanying EDS spectra. A. Secondary electron image of a euxinic sample from 53.61 m depth, showing a small pyrite framboid. B. Backscatter image of a euxinic sample from 53.61 m depth, showing a small pyrite framboid. C. Backscatter image of a ferruginous sample from 51.04 m depth, showing an agglomeration of pyrite framboids and disordered euhedral pyrite. The EDS spectra for all three samples confirm unoxidised pyrite, with background CaCO_3 also recorded for samples A and B.

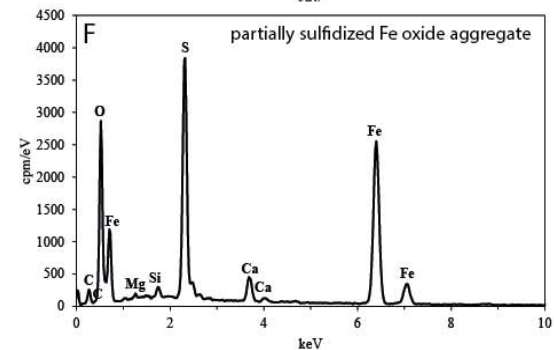
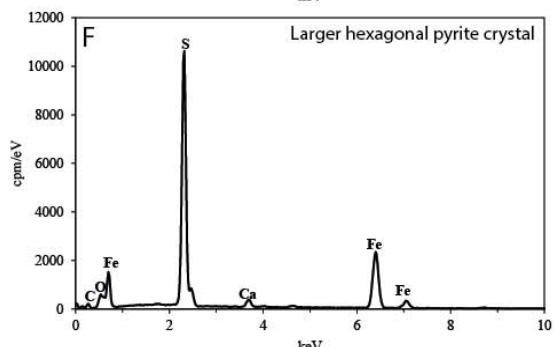
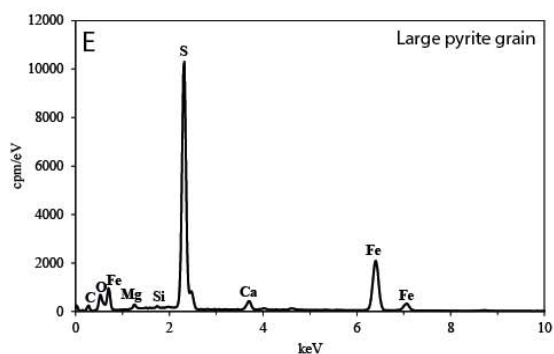
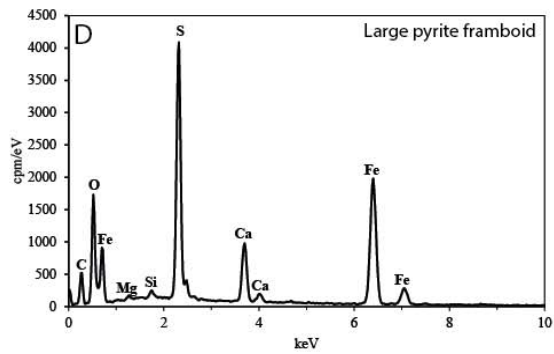
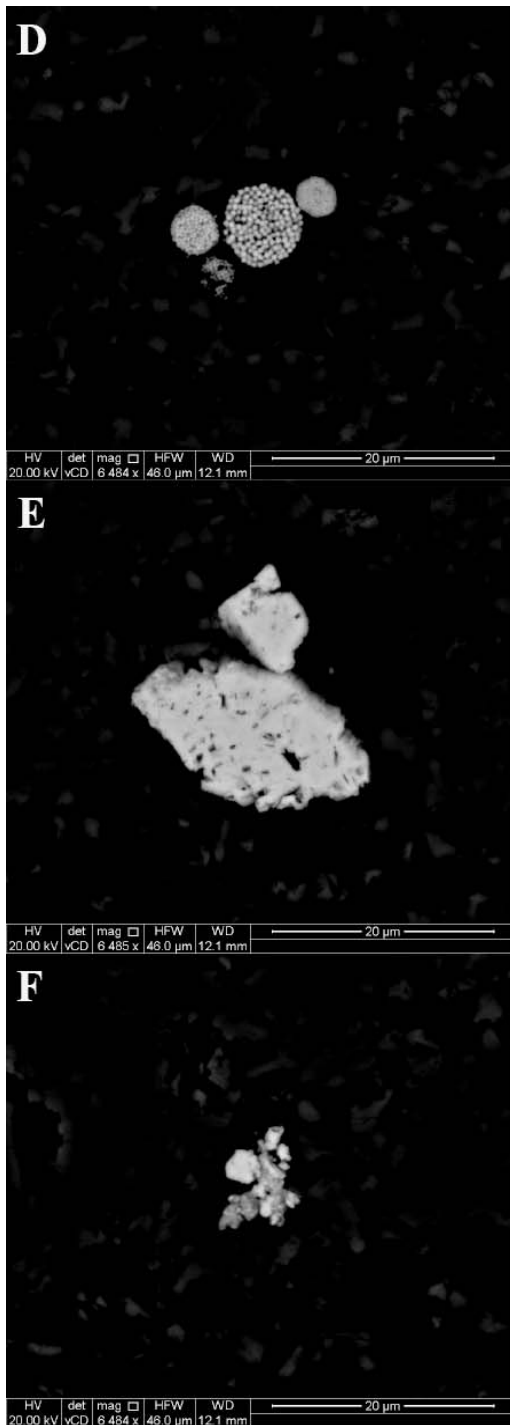


Figure DR5 contd. D. Backscatter image of a ferruginous sample from 53.25 m depth, showing a small pyrite framboid. E. Backscatter image of a ferruginous sample from 53.25 m depth, showing a large pyrite grain. F. Backscatter image of a ferruginous sample from 53.25 m depth, showing a partially sulfidized Fe oxide aggregate. The EDS spectra also show minor CaCO_3 for all samples.

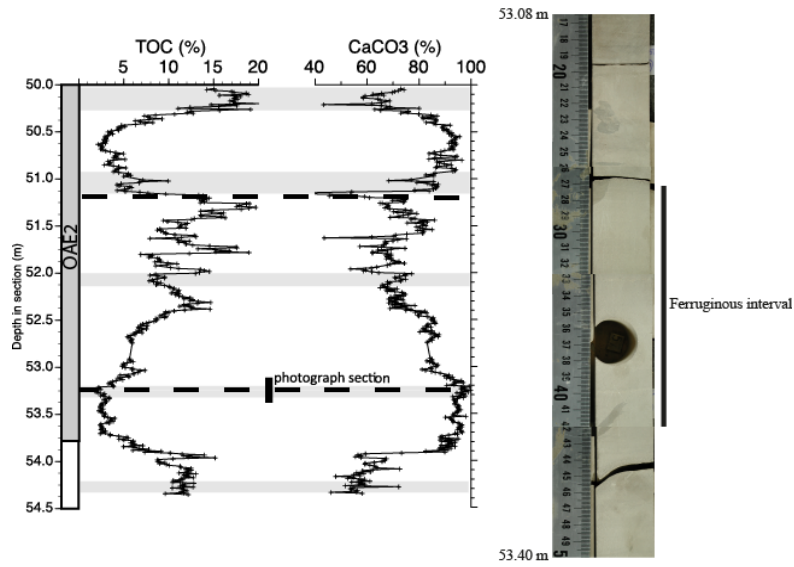


Figure DR6. Composite photograph of a ferruginous interval, with euxinic depositional conditions above and below, and CaCO₃ and TOC contents through the entire studied interval.

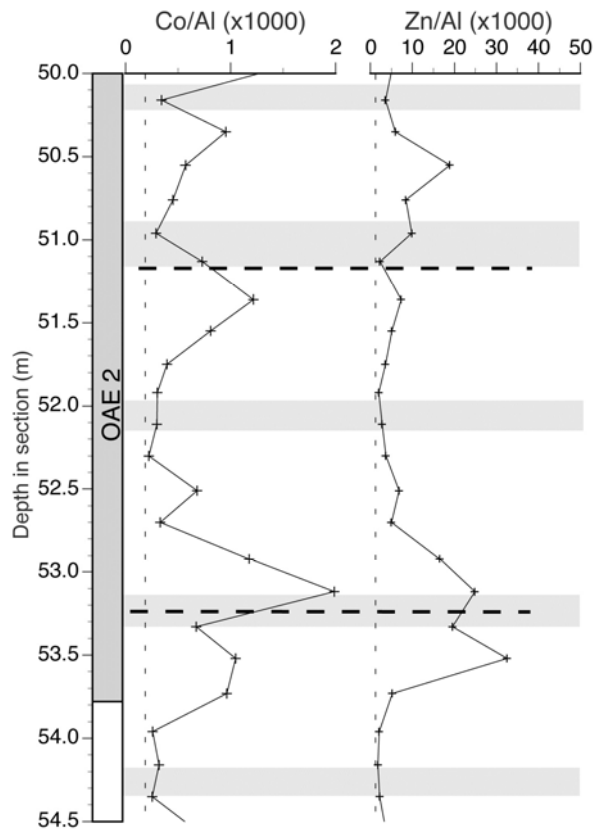


Figure DR7. Co/Al and Zn/Al ratios during the onset of OAE2 at Tarfaya S57. Dashed lines represent ratios in average shale (0.21 for Co/Al and 1.07 for Zn/Al).

Continental weathering

The ratios of K/Al and K/Si can be used to evaluate relative changes in continental weathering intensity. The use of K/Al or K/Si ratios as proxies for continental weathering is based on the enhanced leaching of cations from rocks on land, and the formation of secondary clay minerals (Singer, 1980; Weaver, 1989): The more intense chemical weathering becomes (usually as temperature, atmospheric $p\text{CO}_2$ and precipitation increase), the more K is leached from terrestrial rocks and lost into solution, resulting in lower K/Al ratios in marine sediments (e.g., Zabel et al., 2001). To distinguish between fluvial (i.e., a strong chemical weathering source) and aeolian (i.e., a strong physical weathering source) sediment input, the K/Si ratio has the advantage that K is dominantly bound to fine-grained clay minerals usually transported by rivers, while Si is enriched in the silt and sand fractions of terrestrial sediments and is transported mostly by wind (Wehausen and Brumsack, 2002). Therefore, a higher K/Si ratio indicates a dominance of chemical over physical weathering.

In general, lower K/Al ratios and significantly higher K/Si ratios are evident for ferruginous intervals at the open marine ODP Site 1261 (Figure DR8). However, on continental shelf environments, this direct translation of the continental weathering signal into the marine sediment archive is often disturbed by wave- or current-induced sediment re-suspension in shallow waters, leading to less clear geochemical records as observed for S57 at Tarfaya (Figure DR5). Nevertheless, the fact that low K/Al and high K/Si ratios are evident across ferruginous intervals in the deep ocean sediments of ODP 1261 provides strong support for orbital timescale variability in the intensity of chemical weathering across the subtropical-tropical zone in the Late Cretaceous.

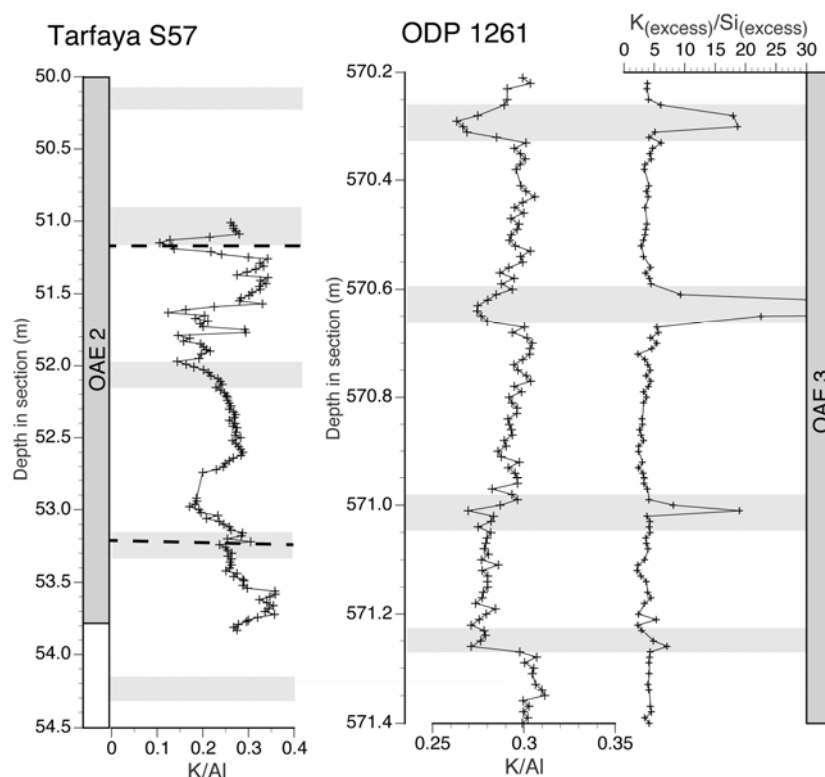


Figure DR8. K/Al and K/Si ratios. A. OAE2 sediments at S57, Tarfaya; B. Coniacian-Santonian OAE3 sediments, ODP Leg 207 at Site 1261, Demerara Rise.

S Isotope and General Circulation Modelling

The S isotope modelling was performed in order to estimate water column sulfate concentrations to evaluate whether any significant changes in seawater sulfate availability

occurred across the ferruginous intervals in the Tarfaya basin. A standard S-isotope box model (Adams et al., 2010), modified to account for high organic S burial fluxes in Cretaceous OAE sediments, was constructed to estimate seawater sulfate concentrations in the proto-North Atlantic during the onset of OAE2, using the following equations:

$$\frac{d}{dt}M_s = F_w + F_v + F_m - (F_{py} + F_{os} + F_{evap}) \quad (1)$$

$$\frac{d}{dt}\delta^{34}S_{sulfate} = \frac{F_w\delta_w + F_v\delta_v + F_m\delta_m - \delta^{34}S_{sulfate}(F_w + F_v + F_m) - F_{py}\Delta^{34}S_{py-sulfate} - F_{os}\Delta^{34}S_{os-sulfate}}{M_s} \quad (2)$$

where F_w represents the weathering input flux and δ_w is its isotopic composition, F_v represents the volcanic input flux and δ_v is its isotopic composition, F_m represents the mantle input flux and δ_m is its isotopic composition, F_{py} is the burial flux of pyrite, F_{os} is the organic sulfur burial flux, F_{evap} is the sulfur evaporite burial flux, $\Delta^{34}S_{py-sulfate}$ is the isotopic fractionation between pyrite and seawater sulfate, $\Delta^{34}S_{os-sulfate}$ is the isotopic fractionation between organic sulfur and seawater sulfate, and M_s represents the mass of sulfate in the ocean. Initial input parameters were based on S isotope analyses from the current study ($\delta^{34}S_{sulfate}$ and $\delta^{34}S_{py}$), and on literature values for the Cretaceous sulfur cycle at steady state (Adams et al., 2010; Aizenshtat and Amrani, 2004), which were then used to estimate sulfate concentrations based on a number of scenarios (outlined below).

In order to estimate the rate of change in $\delta^{34}S_{sulfate}$ at this time we took a 3-point average of the CAS analyses, which gives a reasonable linear up-section increase (Figure DR9). Assuming obliquity forcing of the sedimentary cyclicity (Meyers, 2012) gives a rate of change in $\delta^{34}S_{sulfate}$ of 30‰ Myr⁻¹. Although obliquity forcing appears to be dominant at Tarfaya, eccentricity forcing may also play a role in the sediment cyclicity of core S57 across the study interval (Meyers et al., 2012). If eccentricity is assumed to be the driving influence then our calculated sulfate concentrations would be ~2.4 times higher, which would give maximum sulfate concentrations of ~17 mM. However, since obliquity appears to be dominant over eccentricity at Tarfaya, we here assume that the lower calculated sulfate concentrations presented in the main text are more likely to be representative of concentrations in the Tarfaya basin.

Sulfur flux estimates used in this study are given in Table DR2. An important observation concerns the high concentrations of organic sulfur relative to pyrite sulfur in OAE2 sediments. On the Tarfaya shelf, organic sulfur is around 6 times greater than pyrite sulfur, whereas in the deeper proto-North Atlantic at Demerara Rise, organic sulfur burial is ~3 times greater than pyrite sulfur burial (Hetzl et al., 2009). We have therefore included an organic sulfur term in our isotope model, assuming an isotopic composition for this flux of -7‰ (Aizenshtat et al., 2004), and the model was run with a burial flux of organic sulfur that was either 3 times or 6 times greater than the pyrite burial flux. At steady state, this additional depositional flux of sulfur must be matched by an additional influx. Here, we account for three possible scenarios. In the first scenario, we balance an additional organic sulfur burial flux (3 times the pyrite burial flux) with an increased oceanic influx of sulfur from enhanced continental weathering. An increase in the continental weathering influx by a factor of 3.2 is required to maintain steady state, which is in good agreement with estimates based on Ca isotope systematics of a three-fold increase in global weathering at this time (Blättler et al., 2011). In the second scenario, again for an organic sulfur burial flux of three times the pyrite burial flux, we maintain mass balance by increasing the volcanic sulfur influx by a factor of 7.6. The rationale for this stems from the suggestion of a possible 7-fold increase in volcanic sulfur in the run-up to OAE2 (Adams et al., 2010). In scenario 3, we balance an additional organic sulfur burial flux of 6 times the pyrite burial flux by increasing both the weathering (by a factor of 3.2) and volcanic (by a factor of 7.4) sulfur influxes. Although there is clearly a large degree of uncertainty in the precise magnitude of sulfur fluxes into and out

of the ocean at this time, it is important to note that perturbations to the model (within realistic constraints) have little impact on our conclusions - namely that oceanic sulfur concentrations were lower than at present, with no evidence for fluctuations associated with the observed redox cyclicity (see main text).

An additional important observation relates to spatial variability in estimates for the isotopic composition of seawater sulfate during OAE2, with apparent large disparity between the Pacific and proto-North Atlantic oceans (this study; Ohkouchi et al., 1999; Paytan et al., 2004; Adams et al., 2010). As discussed in the text, this indicates that sulfate concentrations were likely very different in the Pacific and proto-North Atlantic. Thus, modelling the S cycle for the whole ocean based on CAS analyses for the Tarfaya basin is problematic. Instead, we have here chosen to model the proto-Atlantic as a semi-closed system that experienced reduced exchange with the global ocean. Support for this approach comes from modelling a Cretaceous climate simulation using the GENESIS version 3.0 Earth system model coupled to the MOM2 oceanic GCM (Zhou et al., 2008). GENESIS is composed of an atmospheric General Circulation Model (GCM) coupled to multilayer models of vegetation, soil and land ice, and snow (Thompson and Pollard, 1997). In comparison to GENESIS version 2.3, the solar and infrared radiation schemes have been replaced with that used in NCAR's CCM3 (Kiehl et al., 1998). GENESIS–MOM does not currently include a river routing scheme. Continental river runoff is globally averaged and uniformly spread over the world ocean. Such an approximation is appropriate for the Cretaceous where major river drainage basins are not known in detail.

MOM2 is a three-dimensional, z-coordinate ocean GCM and has a horizontal grid spacing of 3.75° , and 20 vertical levels. To ensure conservation of energy and mass, the horizontal grid has been adjusted with a cosine-weighted distortion in order to match the T31 spectral grid used in GENESIS. In our implementation of MOM2, we use an isopycnal mixing scheme (Redi, 1982). Coefficients of horizontal viscosity and diffusion are $2 \times 10^9 \text{ cm}^2 \text{ s}^{-1}$ and $0.5 \times 10^7 \text{ cm}^2 \text{ s}^{-1}$; coefficients of vertical viscosity and diffusion are $1.0 \text{ cm}^2 \text{ s}^{-1}$ and $0.2 \text{ cm}^2 \text{ s}^{-1}$. MOM2 also includes a full convection scheme (Marotzke, 1991; Rahmstorf, 1993), which removes buoyancy instabilities within a water column. Hydrological processes, including precipitation/evaporation, river runoff, and sea ice formation/melt, are calculated in GENESIS and then passed to MOM2. The accumulation of snow on sea ice is tracked in the upper layer. Rain on sea ice is treated as runoff. The GENESIS and MOM models have been fully coupled, exchanging heat, moisture, and momentum fluxes every 6 h. However, in order to make long integrations (N 5000 yr), we have developed an alternating synchronous–asynchronous coupling technique that works as follows: 1. Fully coupled synchronous segments of 35 yr are run, with atmospheric–ocean exchanges performed at each OGCM time step of 6 h. During the last 10 yr of each segment, monthly mean near-surface meteorology such as air temperature, humidity, winds, downward solar and infrared radiative fluxes, and precipitation were stored as 10-year averages; 2. Following each synchronous segment, the saved fluxes are then used to drive the OGCM alone through the next asynchronous segment of 500–2000 yr, with ocean surface fluxes calculated by the AGCM's land surface transfer scheme boundary layer routine using the previously saved atmospheric conditions and the current OGCM sea-surface temperatures. Sea ice is considered part of the AGCM, and where sea ice exists in the synchronous segments, all saved “surface meteorological” quantities are those at the sea ice base; 3. A final 35-year fully coupled synchronous segment is completed to produce data for analyses. This synchronous–asynchronous scheme has already been applied to approach equilibrium in previous work (Kim et al., 2003; Voss and Sausen, 1996). Simulations were integrated through at least 4 asynchronous–asynchronous segments, representing integration durations of more than 6000 yr. After these long integrations, the ocean is very close to equilibrium. Global average temperature trends are 0.15°C/ka . In the upper ocean (top 25 m), seawater temperature trends are 0.08°C/ka .

The model was run with a Cretaceous geography and topography representing Cenomanian lowstand conditions (Poulsen et al., 2007). The GCM simulation with Cretaceous boundary conditions yields data regarding exchange fluxes of the North-Atlantic with the Pacific (Panthalassa) and the eastern Tethys (Figure DR10). The fluxes are depth-integrated (surface to bottom) throughout the water column. Incoming (from Panthalassa and the eastern Tethys) and outgoing fluxes (to the Pacific and the eastern Tethys) of the North Atlantic are summed up and were compared to global fluxes during the Cretaceous simulation. Based on the underlying geography, bathymetry, and the existing uncertainties on those time scales, the N-Atlantic has a volume of 72,915,453 km³. This equals about 21.5% of the world ocean volume at that time, and all of the S flux estimates presented in Table DR2 were adjusted in proportion to this value. The global water fluxes in and out of all existing ocean basins add up to about 363 Sv. The horizontal fluxes across the boundaries between the N-Atlantic and the Pacific, as well as between the North Atlantic and the eastern Tethys, sum up to 28 Sv. Thus, only about 8% of the global horizontal exchange processes take place in the North Atlantic. A number of uncertainties are included in this estimation of an 8% exchange, including sill depth, paleo-water depth and rates of circulation, and changes in some of these parameters would likely act to decrease this exchange rate even further. Nevertheless, this low value justifies our consideration of the proto-North Atlantic as a semi-enclosed system for the purpose of the S-isotope model.

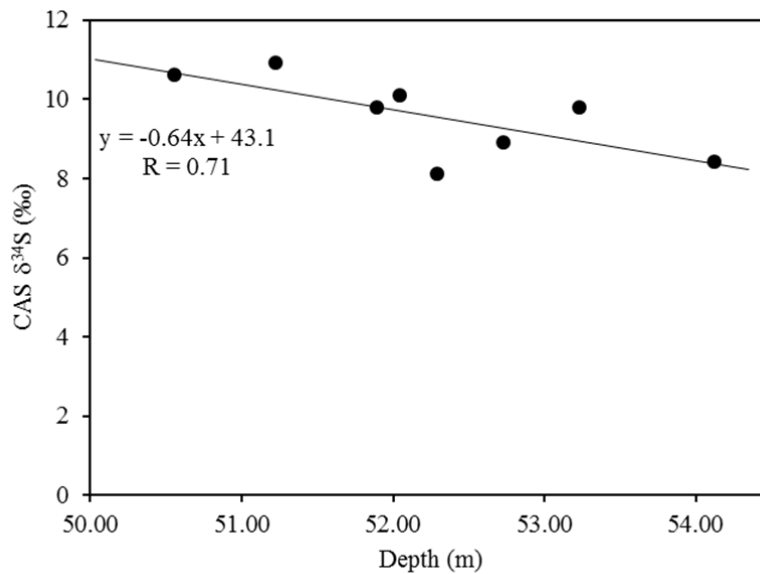


Figure DR9. Carbonate associated sulfate (3-point average) versus depth at S57, Tarfaya. Slope of the line gives the rate of change of the seawater sulfate isotopic composition across the studied interval.

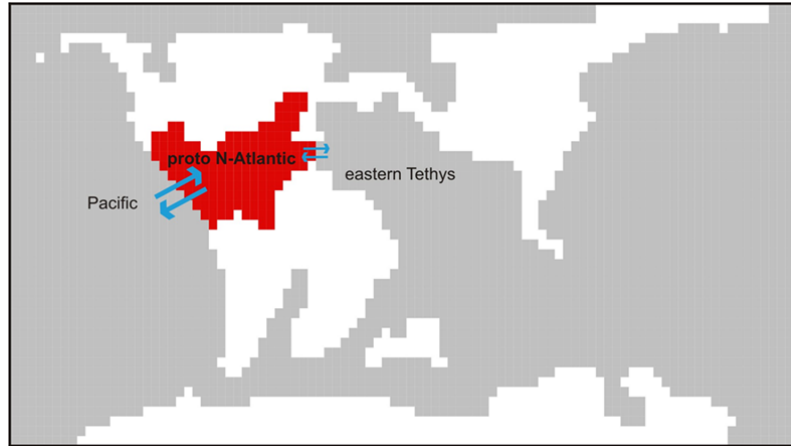


Figure DR10: Map highlighting (in red) the proto North Atlantic on a Mid-Cretaceous paleogeography. Blue arrows highlight the calculated fluxes.

Table DR1. Analytical data.

| Depth (m) | CaCO ₃ (wt%) | TOC (wt%) | S _{tot} (wt%) | Fe _{AVS} (wt%) | Fe _{py} (wt%) | Fe _{carb} (wt%) | Fe _{ox} (wt%) | Fe _{mag} (wt%) | Fe _T (wt%) | Al (wt%) | P (wt%) | δ ³⁴ S _{py} (‰) | δ ³⁴ S _{CAS} (‰) |
|--------------|----------------------------|--------------|---------------------------|----------------------------|---------------------------|-----------------------------|---------------------------|----------------------------|--------------------------|-------------|------------|--|---|
| 50.04 | 72.89 | 15.04 | 2.75 | 0.011 | 0.231 | 0.023 | 0.053 | 0.003 | 0.44 | 0.49 | 0.093 | -22.7 | |
| 50.06 | 72.05 | 15.21 | 2.82 | 0.013 | 0.205 | 0.020 | 0.067 | 0.002 | 0.39 | 0.48 | 0.072 | -22.2 | |
| 50.10 | 62.14 | 18.86 | 3.60 | 0.022 | 0.304 | 0.023 | 0.197 | 0.006 | 0.71 | 0.79 | 0.094 | -25.4 | |
| 50.12 | 59.23 | 18.01 | 3.44 | 0.015 | 0.338 | 0.030 | 0.164 | 0.003 | 0.76 | 1.00 | 0.071 | -24.3 | |
| 50.14 | 58.48 | 17.28 | 5.02 | 0.011 | 0.719 | 0.039 | 0.864 | 0.027 | 1.82 | 1.09 | 0.047 | -13.7 | |
| 50.16 | 64.89 | 17.28 | 3.31 | 0.004 | 0.196 | 0.021 | 0.187 | 0.004 | 0.66 | 0.79 | 0.056 | -25.5 | |
| 50.18 | 67.06 | 17.17 | 3.28 | 0.005 | 0.229 | 0.018 | 0.184 | 0.004 | 0.57 | 0.57 | 0.043 | -27.1 | |
| 50.20 | 61.89 | 20.03 | 3.74 | 0.007 | 0.222 | 0.014 | 0.180 | 0.001 | 0.59 | 0.63 | 0.048 | -27.7 | |
| 50.22 | 65.39 | 17.56 | 3.76 | 0.005 | 0.318 | 0.045 | 0.116 | 0.012 | 0.85 | 0.93 | 0.059 | -17.4 | 10.0 |
| 50.24 | 67.22 | 12.38 | 8.27 | 0.009 | 3.790 | 0.134 | 0.172 | 0.053 | 4.46 | 0.63 | 0.045 | -3.3 | |
| 50.26 | 62.89 | 19.09 | 4.09 | 0.004 | 0.527 | 0.045 | 0.128 | 0.010 | 0.90 | 0.98 | 0.071 | -17.7 | |
| 50.28 | 75.89 | 12.51 | 2.66 | 0.000 | 0.361 | 0.036 | 0.072 | 0.008 | 0.63 | 0.74 | 0.065 | | |
| 50.30 | 72.97 | 12.71 | 2.82 | 0.000 | 0.333 | 0.045 | 0.091 | 0.007 | 0.72 | 0.77 | 0.048 | -18.6 | |
| 50.32 | 84.48 | 8.54 | 2.34 | 0.000 | 0.502 | 0.069 | 0.137 | 0.014 | 0.78 | 0.37 | 0.035 | | |
| 50.34 | 81.33 | 7.72 | 1.60 | 0.007 | 0.283 | 0.034 | 0.050 | 0.003 | 0.45 | 0.41 | 0.027 | -15.1 | |
| 50.36 | 81.53 | 9.25 | 1.51 | 0.004 | 0.231 | 0.044 | 0.034 | 0.001 | 0.38 | 0.44 | 0.028 | | |
| 50.38 | 86.51 | 6.27 | 1.17 | 0.005 | 0.215 | 0.035 | 0.036 | 0.004 | 0.33 | 0.39 | 0.026 | | |
| 50.40 | 82.58 | 8.23 | 1.46 | 0.004 | 0.111 | 0.043 | 0.031 | 0.001 | 0.35 | 0.48 | 0.029 | -17.4 | |
| 50.42 | 86.52 | 6.29 | 1.16 | 0.004 | 0.192 | 0.032 | 0.022 | 0.002 | 0.28 | 0.36 | 0.022 | | |
| 50.44 | 89.33 | 5.13 | 1.05 | 0.000 | 0.151 | 0.026 | 0.029 | 0.002 | 0.23 | 0.30 | 0.021 | -17.5 | |
| 50.46 | 89.06 | 4.74 | 0.95 | 0.000 | 0.003 | 0.033 | 0.027 | 0.006 | 0.25 | 0.28 | 0.021 | | |
| 50.48 | 89.36 | 4.43 | 0.86 | 0.000 | 0.170 | 0.028 | 0.038 | 0.002 | 0.26 | 0.30 | 0.018 | | |
| 50.50 | 90.87 | 3.24 | 0.65 | 0.000 | 0.140 | 0.024 | 0.025 | 0.007 | 0.22 | 0.27 | 0.018 | -16.1 | |
| 50.52 | 91.48 | 3.76 | 0.69 | 0.000 | 0.113 | 0.022 | 0.036 | 0.001 | 0.18 | 0.22 | 0.015 | | |
| 50.54 | 92.27 | 3.20 | 0.61 | 0.000 | 0.118 | 0.026 | 0.030 | 0.001 | 0.19 | 0.22 | 0.014 | | |
| 50.56 | 94.04 | 3.01 | 0.68 | 0.000 | 0.115 | 0.019 | 0.042 | 0.002 | 0.18 | 0.17 | 0.014 | -18.4 | 10.9 |
| 50.58 | 94.02 | 2.77 | 0.60 | 0.000 | 0.112 | 0.023 | 0.041 | 0.001 | 0.18 | 0.17 | 0.013 | | |
| 50.60 | 92.35 | 2.95 | 0.62 | 0.000 | 0.112 | 0.024 | 0.043 | 0.000 | 0.19 | 0.21 | 0.014 | | |
| 50.62 | 91.53 | 2.95 | 0.71 | 0.000 | 0.197 | 0.029 | 0.056 | 0.003 | 0.30 | 0.29 | 0.015 | -12.7 | |
| 50.64 | 93.95 | 2.37 | 0.58 | 0.000 | 0.118 | 0.022 | 0.039 | 0.002 | 0.19 | 0.25 | 0.013 | | |
| 50.66 | 92.81 | 2.62 | 0.66 | 0.000 | 0.115 | 0.023 | 0.036 | 0.000 | 0.20 | 0.26 | 0.013 | | |
| 50.68 | 91.70 | 2.42 | 0.56 | 0.000 | 0.122 | 0.022 | 0.044 | 0.000 | 0.19 | 0.23 | 0.013 | -16.1 | |
| 50.70 | 89.81 | 2.99 | 0.71 | 0.000 | 0.162 | 0.031 | 0.054 | 0.001 | 0.25 | 0.34 | 0.016 | | |
| 50.72 | 85.77 | 4.09 | 0.84 | 0.002 | 0.174 | 0.031 | 0.054 | 0.001 | 0.32 | 0.48 | 0.022 | | |
| 50.74 | 86.47 | 4.36 | 0.83 | 0.000 | 0.195 | 0.039 | 0.046 | 0.000 | 0.31 | 0.40 | 0.021 | -20.9 | |
| 50.76 | 94.50 | 4.08 | 0.88 | 0.000 | 0.149 | 0.026 | 0.047 | 0.003 | 0.26 | 0.35 | 0.018 | | |
| 50.78 | 85.82 | 4.21 | 0.80 | 0.000 | 0.207 | 0.028 | 0.049 | 0.007 | 0.29 | 0.32 | 0.018 | -21.5 | 10.9 |
| 50.80 | 96.39 | 3.83 | 0.89 | 0.000 | 0.139 | 0.032 | 0.023 | 0.002 | 0.24 | 0.34 | 0.024 | | |
| 50.82 | 86.82 | 3.49 | 0.61 | 0.000 | 0.154 | 0.027 | 0.035 | 0.005 | 0.22 | 0.29 | 0.022 | | |
| 50.84 | 89.53 | 3.40 | 0.59 | 0.000 | 0.100 | 0.019 | 0.034 | 0.001 | 0.18 | 0.21 | 0.020 | -21.6 | |
| 50.86 | 90.58 | 3.84 | 0.69 | 0.000 | 0.122 | 0.020 | 0.032 | 0.004 | 0.20 | 0.25 | 0.023 | | |
| 50.88 | 86.28 | 5.21 | 1.04 | 0.000 | 0.145 | 0.026 | 0.055 | 0.002 | 0.26 | 0.36 | 0.021 | -22.2 | |
| 50.90 | 94.11 | 4.22 | 0.94 | 0.000 | 0.092 | 0.016 | 0.114 | 0.006 | 0.25 | 0.33 | 0.018 | -22.0 | |
| 50.92 | 93.04 | 3.84 | 0.60 | 0.000 | 0.078 | 0.016 | 0.079 | 0.000 | 0.18 | 0.23 | 0.016 | -22.3 | |
| 50.94 | 86.12 | 5.48 | 1.06 | 0.000 | 0.109 | 0.012 | 0.102 | 0.000 | 0.28 | 0.40 | 0.022 | -22.0 | |
| 50.96 | 82.56 | 5.77 | 1.06 | 0.000 | 0.149 | 0.015 | 0.071 | 0.006 | 0.28 | 0.42 | 0.025 | -23.6 | |
| 51.01 | 76.91 | 7.10 | 1.69 | 0.000 | 0.335 | 0.034 | 0.114 | 0.007 | 0.58 | 0.97 | 0.011 | -24.5 | |
| 51.03 | 85.55 | 6.74 | 1.61 | 0.000 | 0.256 | 0.026 | 0.152 | 0.008 | 0.55 | 0.95 | 0.013 | -26.2 | |
| 51.05 | 83.31 | 4.70 | 0.92 | 0.000 | 0.132 | 0.016 | 0.119 | 0.003 | 0.31 | 0.50 | 0.007 | -24.6 | 10.6 |
| 51.07 | 84.90 | 4.50 | 0.85 | 0.000 | 0.110 | 0.017 | 0.095 | 0.001 | 0.26 | 0.41 | 0.006 | -23.5 | |
| 51.09 | 86.64 | 5.86 | 1.32 | 0.000 | 0.103 | 0.016 | 0.134 | 0.006 | 0.32 | 0.44 | 0.009 | -23.1 | |
| 51.11 | 85.41 | 5.10 | 1.08 | 0.000 | 0.190 | 0.032 | 0.077 | 0.009 | 0.40 | 0.65 | 0.011 | -23.2 | |
| 51.13 | 83.86 | 5.17 | 2.47 | 0.000 | 0.981 | 0.082 | 0.193 | 0.031 | 1.33 | 1.82 | 0.026 | -7.1 | |
| 51.15 | 36.46 | 7.70 | 11.94 | 0.000 | 3.504 | 0.368 | 2.334 | 0.137 | 9.29 | 3.00 | 0.048 | -2.1 | |
| 51.17 | 53.40 | 13.32 | 5.96 | 0.000 | 1.843 | 0.211 | 1.146 | 0.071 | 3.43 | 2.65 | 0.071 | -10.2 | |
| 51.19 | 59.06 | 13.15 | 4.34 | 0.000 | 1.319 | 0.146 | 0.772 | 0.046 | 2.35 | 2.60 | 0.081 | -12.0 | |
| 51.21 | 74.74 | 13.44 | 2.79 | 0.000 | 0.573 | 0.044 | 0.143 | 0.012 | 0.79 | 1.00 | 0.058 | -21.7 | |
| 51.23 | 69.72 | 13.65 | 2.79 | 0.000 | 0.481 | 0.041 | 0.142 | 0.010 | 0.72 | 0.76 | 0.044 | -21.6 | 11.4 |
| 51.25 | 73.97 | 13.50 | 2.47 | 0.000 | 0.322 | 0.029 | 0.083 | 0.009 | 0.50 | 0.54 | 0.046 | | |
| 51.26 | 64.89 | 18.98 | 3.17 | 0.009 | 0.266 | 0.026 | 0.085 | 0.008 | 0.45 | 0.67 | 0.092 | | |
| 51.29 | 67.97 | 17.53 | 3.30 | 0.000 | 0.381 | 0.033 | 0.122 | 0.009 | 0.59 | 0.62 | 0.138 | -21.0 | |
| 51.31 | 66.72 | 18.93 | 3.21 | 0.005 | 0.254 | 0.021 | 0.072 | 0.006 | 0.44 | 0.58 | 0.108 | | |
| 51.33 | 74.64 | 14.83 | 2.62 | 0.000 | 0.172 | 0.024 | 0.060 | 0.002 | 0.33 | 0.42 | 0.049 | | |
| 51.35 | 70.22 | 14.73 | 2.44 | 0.000 | 0.193 | 0.020 | 0.069 | 0.002 | 0.35 | 0.41 | 0.036 | -26.2 | |
| 51.37 | 79.14 | 15.78 | 2.84 | 0.000 | 0.227 | 0.028 | 0.054 | 0.003 | 0.40 | 0.46 | 0.050 | | |
| 51.39 | 73.80 | 13.62 | 2.37 | 0.000 | 0.228 | 0.020 | 0.065 | 0.006 | 0.37 | 0.44 | 0.071 | | |
| 51.41 | 68.89 | 16.30 | 2.86 | 0.000 | 0.229 | 0.023 | 0.060 | 0.006 | 0.41 | 0.52 | 0.038 | -23.1 | |
| 51.43 | 76.89 | 12.53 | 2.15 | 0.000 | 0.175 | 0.022 | 0.071 | 0.001 | 0.31 | 0.33 | 0.063 | | |
| 51.45 | 80.52 | 9.85 | 1.68 | 0.000 | 0.159 | 0.018 | 0.051 | 0.002 | 0.27 | 0.29 | 0.040 | | |
| 51.47 | 75.39 | 12.09 | 2.09 | 0.000 | 0.208 | 0.021 | 0.058 | 0.000 | 0.33 | 0.33 | 0.069 | -20.6 | |

| | | | | | | | | | | | | | |
|-------|-------|-------|-------|-------|-------|-------|-------|-------|-------|------|-------|-------|------|
| 51.49 | 81.38 | 11.37 | 1.94 | 0.000 | 0.164 | 0.029 | 0.047 | 0.003 | 0.29 | 0.31 | 0.029 | | |
| 51.51 | 78.80 | 11.18 | 1.71 | 0.000 | 0.164 | 0.029 | 0.045 | 0.000 | 0.30 | 0.34 | 0.029 | | |
| 51.53 | 81.44 | 9.02 | 1.46 | 0.000 | 0.151 | 0.025 | 0.048 | 0.000 | 0.28 | 0.35 | 0.022 | -27.5 | |
| 51.55 | 79.33 | 9.16 | 1.45 | 0.000 | 0.186 | 0.027 | 0.055 | 0.001 | 0.35 | 0.45 | 0.023 | | |
| 51.57 | 81.31 | 9.70 | 1.61 | 0.000 | 0.174 | 0.028 | 0.062 | 0.002 | 0.33 | 0.32 | 0.022 | | |
| 51.59 | 75.22 | 10.67 | 1.88 | 0.000 | 0.336 | 0.038 | 0.081 | 0.005 | 0.52 | 0.72 | 0.014 | -25.9 | |
| 51.61 | 70.31 | 13.05 | 3.60 | 0.000 | 1.097 | 0.063 | 0.211 | 0.020 | 1.51 | 1.27 | 0.081 | | |
| 51.63 | 43.49 | 7.90 | 17.34 | 0.000 | 5.308 | 0.526 | 1.752 | 0.189 | 15.03 | 1.37 | 0.005 | | |
| 51.65 | 71.72 | 11.04 | 2.21 | 0.000 | 0.419 | 0.043 | 0.089 | 0.005 | 0.68 | 1.17 | 0.020 | -21.8 | |
| 51.67 | 66.81 | 11.10 | 2.64 | 0.000 | 0.953 | 0.059 | 0.146 | 0.011 | 1.26 | 1.45 | 0.029 | | |
| 51.69 | 67.22 | 11.90 | 2.44 | 0.000 | 0.628 | 0.051 | 0.127 | 0.005 | 0.97 | 1.44 | 0.031 | | |
| 51.71 | 66.47 | 14.55 | 3.24 | 0.000 | 0.963 | 0.057 | 0.194 | 0.010 | 1.35 | 1.63 | 0.070 | -21.8 | |
| 51.73 | 65.47 | 17.58 | 3.80 | 0.000 | 0.822 | 0.055 | 0.179 | 0.008 | 1.20 | 1.36 | 0.094 | | |
| 51.75 | 69.14 | 15.18 | 2.79 | 0.000 | 0.370 | 0.034 | 0.109 | 0.002 | 0.63 | 0.82 | 0.046 | | |
| 51.77 | 67.81 | 15.22 | 2.84 | 0.000 | 0.375 | 0.039 | 0.120 | 0.002 | 0.67 | 1.03 | 0.036 | -27.8 | 10.7 |
| 51.79 | 62.06 | 12.29 | 3.13 | 0.000 | 0.792 | 0.058 | 0.266 | 0.015 | 1.24 | 1.95 | 0.150 | | |
| 51.81 | 67.20 | 8.19 | 1.88 | 0.000 | 0.587 | 0.050 | 0.092 | 0.004 | 0.89 | 1.65 | 0.055 | | |
| 51.83 | 67.64 | 7.79 | 1.75 | 0.000 | 0.407 | 0.045 | 0.077 | 0.004 | 0.78 | 1.73 | 0.083 | -28.7 | |
| 51.85 | 67.42 | 8.97 | 1.78 | 0.000 | 0.428 | 0.046 | 0.054 | 0.000 | 0.72 | 1.51 | 0.089 | | |
| 51.87 | 69.89 | 9.14 | 1.82 | 0.000 | 0.476 | 0.048 | 0.071 | 0.002 | 0.77 | 1.51 | 0.043 | -31.8 | 7.1 |
| 51.89 | 70.49 | 9.88 | 2.01 | 0.000 | 0.489 | 0.055 | 0.063 | 0.002 | 0.76 | 1.38 | 0.056 | | |
| 51.90 | 74.30 | 10.92 | 2.28 | 0.000 | 0.441 | 0.051 | 0.076 | 0.002 | 0.74 | 1.27 | 0.059 | | 12.9 |
| 51.92 | 67.74 | 8.53 | 1.79 | 0.000 | 0.435 | 0.044 | 0.056 | 0.000 | 0.73 | 1.75 | 0.038 | | |
| 51.95 | 61.64 | 11.09 | 2.54 | 0.000 | 0.624 | 0.053 | 0.080 | 0.004 | 0.93 | 1.98 | 0.053 | -27.3 | 9.3 |
| 51.97 | 59.48 | 13.96 | 3.60 | 0.000 | 1.282 | 0.086 | 0.182 | 0.009 | 1.75 | 2.61 | 0.065 | | |
| 51.99 | 61.81 | 13.41 | 2.98 | 0.000 | 0.808 | 0.037 | 0.188 | 0.008 | 1.23 | 1.92 | 0.071 | -33.1 | 9.8 |
| 52.01 | 77.14 | 8.53 | 1.48 | 0.011 | 0.512 | 0.028 | 0.358 | 0.004 | 1.08 | 1.43 | 0.358 | | |
| 52.03 | 74.75 | 8.80 | 1.82 | 0.000 | 0.224 | 0.021 | 0.100 | 0.000 | 0.47 | 1.19 | 0.024 | -31.3 | |
| 52.05 | 70.55 | 9.51 | 2.10 | 0.006 | 0.368 | 0.029 | 0.208 | 0.002 | 0.75 | 1.25 | 0.062 | -24.4 | 8.7 |
| 52.07 | 74.85 | 8.20 | 1.52 | 0.000 | 0.391 | 0.030 | 0.236 | 0.000 | 0.81 | 1.39 | 0.018 | | |
| 52.09 | 72.96 | 8.31 | 1.48 | 0.000 | 0.295 | 0.019 | 0.111 | 0.000 | 0.58 | 1.44 | 0.015 | -30.3 | |
| 52.11 | 68.89 | 8.75 | 1.97 | 0.000 | 0.342 | 0.020 | 0.153 | 0.003 | 0.70 | 1.56 | 0.021 | -28.9 | |
| 52.13 | 65.81 | 9.51 | 2.01 | 0.000 | 0.280 | 0.031 | 0.244 | 0.009 | 0.90 | 1.78 | 0.018 | -27.0 | 11.9 |
| 52.15 | 67.81 | 10.14 | 1.84 | 0.000 | 0.391 | 0.020 | 0.210 | 0.007 | 0.86 | 1.70 | 0.029 | | |
| 52.17 | 71.47 | 10.50 | 1.75 | 0.000 | 0.302 | 0.022 | 0.118 | 0.006 | 0.69 | 1.56 | 0.033 | -33.7 | 8.2 |
| 52.19 | 70.56 | 11.05 | 0.12 | 0.000 | 0.263 | 0.041 | 0.021 | 0.002 | 0.58 | 1.35 | 0.030 | | |
| 52.21 | 73.39 | 10.30 | 1.61 | 0.000 | 0.258 | 0.044 | 0.021 | 0.000 | 0.57 | 1.28 | 0.034 | | |
| 52.22 | 74.05 | 11.16 | 1.62 | 0.007 | 0.247 | 0.041 | 0.017 | 0.001 | 0.50 | 1.14 | 0.035 | | |
| 52.24 | 70.81 | 11.14 | 1.64 | 0.000 | 0.242 | 0.043 | 0.017 | 0.002 | 0.50 | 1.10 | 0.032 | -32.3 | |
| 52.26 | 68.97 | 12.38 | 1.63 | 0.010 | 0.157 | 0.030 | 0.011 | 0.000 | 0.41 | 1.04 | 0.051 | | |
| 52.28 | 68.31 | 12.67 | 1.65 | 0.000 | 0.138 | 0.028 | 0.009 | 0.000 | 0.38 | 0.99 | 0.049 | | |
| 52.30 | 68.97 | 13.26 | 1.68 | 0.000 | 0.139 | 0.031 | 0.009 | 0.007 | 0.39 | 0.94 | 0.079 | -34.9 | 7.1 |
| 52.32 | 68.31 | 13.19 | 1.71 | 0.000 | 0.120 | 0.030 | 0.011 | 0.005 | 0.39 | 0.94 | 0.052 | | |
| 52.34 | 69.56 | 12.28 | 1.55 | 0.000 | 0.137 | 0.027 | 0.000 | 0.007 | 0.33 | 0.84 | 0.041 | | |
| 52.36 | 70.47 | 12.67 | 1.66 | 0.000 | 0.158 | 0.031 | 0.014 | 0.008 | 0.36 | 0.81 | 0.029 | | |
| 52.38 | 68.72 | 14.58 | 1.82 | 0.012 | 0.102 | 0.023 | 0.010 | 0.007 | 0.31 | 0.68 | 0.034 | | |
| 52.40 | 74.89 | 10.59 | 1.44 | 0.010 | 0.131 | 0.036 | 0.017 | 0.007 | 0.33 | 0.67 | 0.031 | | |
| 52.42 | 78.43 | 10.00 | 1.46 | 0.000 | 0.127 | 0.035 | 0.030 | 0.003 | 0.37 | 0.74 | 0.054 | -30.1 | |
| 52.44 | 80.87 | 9.56 | 1.54 | 0.000 | 0.217 | 0.037 | 0.042 | 0.008 | 0.52 | 0.78 | 0.126 | | |
| 52.46 | 79.85 | 9.71 | 1.47 | 0.000 | 0.171 | 0.031 | 0.028 | 0.006 | 0.35 | 0.70 | 0.032 | | |
| 52.48 | 85.38 | 8.54 | 1.31 | 0.000 | 0.136 | 0.026 | 0.027 | 0.003 | 0.27 | 0.45 | 0.029 | | |
| 52.50 | 84.62 | 8.60 | 1.28 | 0.000 | 0.137 | 0.027 | 0.025 | 0.006 | 0.29 | 0.45 | 0.033 | | |
| 52.52 | 85.28 | 7.83 | 1.18 | 0.000 | 0.112 | 0.024 | 0.029 | 0.004 | 0.25 | 0.47 | 0.025 | | |
| 52.54 | 86.18 | 7.11 | 1.09 | 0.000 | 0.123 | 0.024 | 0.024 | 0.004 | 0.25 | 0.48 | 0.018 | -24.7 | 9.1 |
| 52.56 | 83.01 | 7.63 | 1.13 | 0.000 | 0.145 | 0.026 | 0.023 | 0.008 | 0.30 | 0.64 | 0.026 | | |
| 52.58 | 84.54 | 6.64 | 0.98 | 0.000 | 0.123 | 0.022 | 0.025 | 0.007 | 0.26 | 0.61 | 0.062 | | |
| 52.60 | 82.73 | 6.98 | 1.10 | 0.000 | 0.180 | 0.026 | 0.040 | 0.009 | 0.36 | 0.74 | 0.025 | | |
| 52.62 | 84.85 | 6.37 | 1.00 | 0.000 | 0.145 | 0.023 | 0.030 | 0.005 | 0.31 | 0.67 | 0.017 | | |
| 52.64 | 85.78 | 6.10 | 0.94 | 0.000 | 0.118 | 0.019 | 0.027 | 0.004 | 0.26 | 0.62 | 0.012 | -17.0 | 5.9 |
| 52.66 | 87.66 | 5.72 | 0.81 | 0.000 | 0.094 | 0.014 | 0.010 | 0.002 | 0.19 | 0.53 | 0.016 | | |
| 52.68 | 87.31 | 5.46 | 0.77 | 0.000 | 0.086 | 0.012 | 0.013 | 0.002 | 0.20 | 0.55 | 0.013 | | |
| 52.70 | 84.97 | 5.95 | 0.86 | 0.000 | 0.112 | 0.016 | 0.016 | 0.021 | 0.23 | 0.62 | 0.016 | | |
| 52.72 | 85.03 | 5.78 | 0.86 | 0.000 | 0.113 | 0.019 | 0.019 | 0.006 | 0.24 | 0.65 | 0.015 | | |
| 52.74 | 83.02 | 5.95 | 0.89 | 0.000 | 0.131 | 0.026 | 0.033 | 0.008 | 0.32 | 0.76 | 0.009 | | 13.2 |
| 52.92 | 84.86 | 5.59 | 0.93 | 0.000 | 0.094 | 0.017 | 0.016 | 0.006 | 0.24 | 0.72 | 0.006 | | |
| 52.94 | 82.88 | 6.02 | 0.94 | 0.000 | 0.155 | 0.023 | 0.028 | 0.010 | 0.32 | 0.72 | 0.007 | | |
| 52.96 | 85.33 | 4.95 | 0.84 | 0.000 | 0.123 | 0.019 | 0.020 | 0.005 | 0.26 | 0.59 | 0.008 | -17.7 | 10.2 |
| 52.98 | 87.11 | 4.84 | 0.77 | 0.000 | 0.101 | 0.015 | 0.010 | 0.004 | 0.20 | 0.51 | 0.006 | | |
| 53.00 | 86.42 | 5.18 | 0.90 | 0.000 | 0.136 | 0.020 | 0.029 | 0.006 | 0.27 | 0.53 | 0.010 | | |
| 53.02 | 84.58 | 5.90 | 0.92 | 0.000 | 0.106 | 0.020 | 0.026 | 0.005 | 0.25 | 0.56 | 0.007 | -17.3 | 9.7 |
| 53.04 | 82.42 | 6.78 | 1.24 | 0.000 | 0.199 | 0.034 | 0.044 | 0.010 | 0.38 | 0.62 | 0.014 | | |
| 53.06 | 86.17 | 6.10 | 0.93 | 0.000 | 0.062 | 0.013 | 0.007 | 0.001 | 0.18 | 0.46 | 0.013 | | |
| 53.08 | | 4.61 | 1.03 | 0.000 | 0.055 | 0.011 | 0.005 | 0.000 | 0.15 | 0.33 | 0.008 | | |
| 53.10 | 89.71 | 5.57 | 0.81 | 0.000 | 0.068 | 0.015 | 0.013 | 0.000 | 0.14 | 0.27 | 0.022 | -25.2 | |
| 53.12 | 90.47 | 4.61 | 0.73 | 0.000 | 0.087 | 0.013 | 0.011 | 0.000 | 0.15 | 0.28 | 0.011 | | |

| | | | | | | | | | | | | | |
|-------|-------|-------|------|-------|-------|-------|-------|-------|------|------|-------|-------|------|
| 53.14 | 93.40 | 4.13 | 0.66 | 0.000 | 0.060 | 0.013 | 0.012 | 0.000 | 0.12 | 0.20 | 0.008 | | |
| 53.16 | 93.71 | 3.55 | 0.67 | 0.000 | 0.084 | 0.009 | 0.021 | 0.002 | 0.14 | 0.18 | 0.011 | -13.9 | |
| 53.18 | 93.20 | 3.61 | 0.68 | 0.000 | 0.073 | 0.007 | 0.036 | 0.001 | 0.15 | 0.21 | 0.016 | -17.5 | |
| 53.20 | 90.58 | 3.87 | 0.63 | 0.000 | 0.071 | 0.007 | 0.033 | 0.003 | 0.16 | 0.30 | 0.014 | -20.5 | |
| 53.22 | 96.24 | 2.24 | 0.40 | 0.000 | 0.038 | 0.002 | 0.041 | 0.002 | 0.10 | 0.13 | 0.012 | -11.3 | |
| 53.24 | 96.08 | 2.37 | 0.40 | 0.000 | 0.047 | 0.008 | 0.029 | 0.002 | 0.10 | 0.14 | 0.012 | -13.0 | 10.6 |
| 53.26 | 96.47 | 1.97 | 0.36 | 0.000 | 0.063 | 0.008 | 0.031 | 0.000 | 0.11 | 0.13 | 0.009 | -7.0 | |
| 53.28 | 94.47 | 2.86 | 0.49 | 0.000 | 0.073 | 0.007 | 0.025 | 0.000 | 0.13 | 0.19 | 0.026 | -7.8 | |
| 53.30 | 95.86 | 2.44 | 0.46 | 0.000 | 0.079 | 0.009 | 0.039 | 0.002 | 0.15 | 0.16 | 0.009 | | |
| 53.32 | 92.91 | 3.39 | 0.58 | 0.000 | 0.080 | 0.005 | 0.038 | 0.001 | 0.16 | 0.23 | 0.012 | -7.7 | |
| 53.33 | 96.98 | 3.40 | 0.63 | | | | | | | | | | |
| 53.34 | 94.73 | 2.77 | 0.53 | 0.000 | 0.086 | 0.007 | 0.025 | 0.001 | 0.14 | 0.18 | 0.010 | -7.2 | |
| 53.36 | 93.53 | 3.08 | 0.53 | 0.000 | 0.089 | 0.011 | 0.020 | 0.002 | 0.17 | 0.22 | 0.008 | -7.8 | |
| 53.38 | 93.99 | 2.60 | 0.49 | 0.000 | 0.115 | 0.011 | 0.020 | 0.000 | 0.17 | 0.21 | 0.007 | | |
| 53.40 | 93.61 | 2.73 | 0.44 | 0.000 | 0.125 | 0.012 | 0.018 | 0.002 | 0.18 | 0.21 | 0.009 | | |
| 53.42 | 95.31 | 2.37 | 0.34 | 0.000 | 0.065 | 0.007 | 0.009 | 0.000 | 0.10 | 0.16 | 0.010 | -5.7 | |
| 53.44 | 94.95 | 2.70 | 0.49 | 0.000 | 0.115 | 0.009 | 0.014 | 0.000 | 0.15 | 0.18 | 0.017 | | |
| 53.46 | 95.93 | 2.22 | 0.46 | 0.000 | 0.101 | 0.006 | 0.010 | 0.000 | 0.16 | 0.15 | 0.009 | | |
| 53.48 | 94.72 | 2.60 | 0.44 | 0.000 | 0.089 | 0.010 | 0.012 | 0.000 | 0.15 | 0.19 | 0.020 | -3.4 | |
| 53.50 | 94.56 | 2.89 | 0.52 | 0.000 | 0.120 | 0.009 | 0.013 | 0.003 | 0.18 | 0.20 | 0.011 | | |
| 53.52 | 93.22 | 2.83 | 0.48 | 0.000 | 0.090 | 0.011 | 0.018 | 0.000 | 0.17 | 0.25 | 0.006 | | |
| 53.54 | 90.06 | 4.00 | 0.76 | 0.000 | 0.117 | 0.012 | 0.029 | 0.000 | 0.22 | 0.31 | 0.012 | -7.2 | |
| 53.56 | 92.32 | 3.56 | 0.67 | 0.000 | 0.151 | 0.012 | 0.034 | 0.000 | 0.25 | 0.27 | 0.013 | | |
| 53.58 | 93.10 | 3.13 | 0.50 | 0.000 | 0.107 | 0.016 | 0.019 | 0.000 | 0.18 | 0.22 | 0.010 | -8.8 | 9.0 |
| 53.60 | 95.00 | 2.48 | 0.51 | 0.000 | 0.136 | 0.013 | 0.015 | 0.000 | 0.19 | 0.18 | 0.012 | | |
| 53.62 | 96.43 | 2.46 | 0.56 | 0.000 | 0.128 | 0.014 | 0.015 | 0.000 | 0.20 | 0.17 | 0.011 | | |
| 53.64 | 96.38 | 2.50 | 0.46 | 0.000 | 0.087 | 0.010 | 0.016 | 0.000 | 0.14 | 0.17 | 0.014 | -8.3 | |
| 53.66 | 95.73 | 2.45 | 0.47 | 0.000 | 0.063 | 0.012 | 0.007 | 0.000 | 0.16 | 0.17 | 0.014 | | |
| 53.68 | 96.18 | 2.59 | 0.43 | 0.000 | 0.060 | 0.010 | 0.007 | 0.000 | 0.11 | 0.17 | 0.017 | | |
| 53.70 | 96.54 | 2.38 | 0.38 | 0.000 | 0.040 | 0.008 | 0.010 | 0.000 | 0.08 | 0.13 | 0.020 | -16.6 | |
| 53.72 | 94.69 | 3.45 | 0.59 | 0.000 | 0.074 | 0.011 | 0.016 | 0.000 | 0.15 | 0.22 | 0.022 | | |
| 53.74 | 88.86 | 5.32 | 0.89 | 0.000 | 0.109 | 0.018 | 0.018 | 0.000 | 0.23 | 0.36 | 0.025 | | |
| 53.76 | | 4.91 | 0.79 | 0.000 | 0.079 | 0.020 | 0.014 | 0.000 | 0.18 | 0.33 | 0.026 | -23.1 | |
| 53.77 | | 5.01 | 0.96 | 0.000 | 0.099 | 0.019 | 0.022 | 0.000 | 0.21 | 0.35 | 0.030 | | |
| 53.79 | | 6.02 | 1.08 | 0.000 | 0.076 | 0.019 | 0.020 | 0.000 | 0.21 | 0.37 | 0.031 | -21.7 | |
| 53.81 | | 6.21 | 1.10 | 0.000 | 0.113 | 0.018 | 0.010 | 0.000 | 0.23 | 0.41 | 0.030 | | |
| 53.83 | | 7.11 | 1.28 | 0.000 | 0.097 | 0.015 | 0.017 | 0.000 | 0.22 | 0.41 | 0.055 | | |
| 53.85 | | 6.24 | 1.13 | 0.000 | 0.077 | 0.006 | 0.014 | 0.000 | 0.15 | 0.17 | 0.102 | | |
| 53.87 | | 7.78 | 1.67 | 0.000 | 0.154 | 0.013 | 0.028 | 0.000 | 0.24 | 0.28 | 0.100 | | |
| 53.89 | | 9.16 | 2.13 | 0.000 | 0.241 | 0.016 | 0.033 | 0.000 | 0.38 | 0.48 | 0.230 | | |
| 53.91 | | 10.16 | 2.35 | 0.000 | 0.299 | 0.016 | 0.038 | 0.000 | 0.43 | 0.52 | 0.132 | -21.8 | |
| 53.93 | 59.39 | 13.97 | 2.87 | 0.000 | 0.501 | 0.038 | 0.104 | 0.006 | 0.89 | 1.10 | 0.224 | | |
| 53.95 | 57.64 | 12.16 | 2.55 | 0.000 | 0.411 | 0.041 | 0.075 | 0.004 | 0.87 | 1.55 | 0.229 | -17.5 | 7.8 |
| 53.96 | 55.48 | 15.16 | 3.24 | | | | | | | | | | |
| 53.97 | 57.56 | 10.48 | 2.39 | 0.000 | 0.536 | 0.050 | 0.078 | 0.005 | 0.98 | 1.73 | 0.239 | | |
| 53.99 | 66.82 | 8.85 | 1.73 | 0.000 | 0.313 | 0.043 | 0.049 | 0.002 | 0.62 | 1.54 | 0.099 | | |
| 54.01 | 65.73 | 9.57 | 2.18 | 0.000 | 0.498 | 0.053 | 0.064 | 0.005 | 0.82 | 1.65 | 0.098 | -22.2 | |
| 54.03 | 59.27 | 9.75 | 6.11 | 0.000 | 2.945 | 0.201 | 0.221 | 0.089 | 3.64 | 1.74 | 0.096 | | |
| 54.05 | 61.06 | 11.26 | 3.82 | 0.000 | 1.387 | 0.112 | 0.158 | 0.041 | 1.77 | 1.71 | 0.124 | | |
| 54.07 | 63.39 | 12.49 | 2.65 | 0.007 | 0.503 | 0.066 | 0.106 | 0.004 | 0.90 | 1.39 | 0.132 | -17.1 | |
| 54.09 | 72.55 | 12.50 | 2.22 | 0.017 | 0.276 | 0.048 | 0.043 | 0.000 | 0.65 | 1.31 | 0.148 | | |
| 54.11 | 58.23 | 12.27 | 2.30 | 0.000 | 0.292 | 0.057 | 0.058 | 0.003 | 0.82 | 1.70 | 0.112 | | |
| 54.13 | 55.98 | 13.03 | 2.50 | 0.006 | 0.383 | 0.067 | 0.080 | 0.002 | 0.91 | 1.73 | 0.137 | -18.5 | 7.9 |
| 54.15 | 54.81 | 12.19 | 2.03 | 0.003 | 0.363 | 0.065 | 0.079 | 0.002 | 0.88 | 1.83 | 0.136 | -17.4 | |
| 54.16 | 57.31 | 11.76 | 2.44 | | | | | | | | | | |
| 54.17 | 47.90 | 12.76 | 2.08 | 0.000 | 0.452 | 0.061 | 0.069 | 0.004 | 1.04 | 2.19 | 0.132 | -15.6 | |
| 54.19 | 52.48 | 11.58 | 1.93 | 0.000 | 0.337 | 0.028 | 0.112 | 0.004 | 0.92 | 2.00 | 0.158 | -14.3 | |
| 54.21 | 56.81 | 11.28 | 1.82 | 0.000 | 0.259 | 0.015 | 0.144 | 0.002 | 0.82 | 1.75 | 0.147 | -18.0 | |
| 54.23 | 54.06 | 12.79 | 1.98 | 0.002 | 0.220 | 0.006 | 0.165 | 0.000 | 0.80 | 1.81 | 0.129 | -14.0 | |
| 54.25 | 56.81 | 11.78 | 1.90 | 0.004 | 0.228 | 0.003 | 0.155 | 0.000 | 0.80 | 1.72 | 0.142 | -17.9 | 9.4 |
| 54.27 | 51.56 | 12.69 | 2.10 | 0.001 | 0.291 | 0.016 | 0.174 | 0.000 | 0.96 | 2.05 | 0.135 | -16.7 | |
| 54.29 | 54.64 | 11.57 | 1.87 | 0.000 | 0.341 | 0.019 | 0.089 | 0.003 | 0.86 | 1.84 | 0.169 | -13.3 | |
| 54.31 | 53.90 | 12.01 | 1.99 | 0.006 | 0.295 | 0.018 | 0.140 | 0.001 | 0.88 | 1.85 | 0.146 | -13.9 | |
| 54.33 | 55.89 | 11.67 | 2.62 | 0.000 | 0.781 | 0.022 | 0.212 | 0.010 | 1.41 | 1.60 | 0.150 | -2.0 | |
| 54.35 | 58.06 | 12.15 | 1.83 | 0.003 | 0.217 | 0.007 | 0.125 | 0.004 | 0.75 | 1.48 | 0.166 | -11.3 | |

Table DR2. Parameters used in the sulfur isotope model. Flux measurements and isotopic values are taken from the literature, with fluxes for Scenarios 1, 2 and 3 scaled to the water volume of the proto-North Atlantic relative to the global ocean during OAE2 (see above text for details). Isotopic values for δ_{py} were taken from the present study as averages measured across intervals corresponding to the three point averages taken for $\delta^{34}\text{S}_{\text{sulfate}}$. F_w represents the weathering input flux and δ_w is the isotopic composition of the weathering input flux, F_v represents the volcanic input flux and δ_v is the isotopic composition of the volcanic input flux, F_m represents the mantle input flux and δ_m is the isotopic composition of the mantle input flux, F_{py} is the burial flux of pyrite, F_{os} is the organic sulfur burial flux and δ_{os} is the organic sulfur burial flux, F_{evap} is the sulfur evaporite burial flux (the isotopic composition of this flux cancels from the mass balance equation given in the main text due to an absence of isotopic fractionation during evaporite formation).

| Literature data for the global ocean | | Ref. |
|--|----------------------------|---|
| $F_w = 0.98 \times 10^{18} \text{ mol Myr}^{-1}$ | $\delta_w = 6\text{‰}$ | Adams et al. (2010); Hansen and Wallmann (2003) |
| $F_v = 0.33 \times 10^{18} \text{ mol Myr}^{-1}$ | $\delta_v = 3\text{‰}$ | Adams et al. (2010); Hansen and Wallmann (2003) |
| $F_m = 0.2 \times 10^{18} \text{ mol Myr}^{-1}$ | $\delta_m = 3.5\text{‰}$ | Adams et al. (2010); Hansen and Wallmann (2003) |
| $F_{py} = 0.68 \times 10^{18} \text{ mol Myr}^{-1}$ | | Adams et al. (2010); Hansen and Wallmann (2003) |
| $F_{\text{evap}} = 0.83 \times 10^{18} \text{ mol Myr}^{-1}$ | | Adams et al. (2010); Hansen and Wallmann (2003) |
| Scenario 1: $F_{os} = 3 \times F_{py}$; $F_w = 3.2 \times \text{modern}$ | | Hetzel et al. (2009); Blättler et al. (2011) |
| $F_w = 0.67 \times 10^{18} \text{ mol Myr}^{-1}$ | $\delta_w = 6\text{‰}$ | |
| $F_v = 0.07 \times 10^{18} \text{ mol Myr}^{-1}$ | $\delta_v = 3\text{‰}$ | |
| $F_m = 0.04 \times 10^{18} \text{ mol Myr}^{-1}$ | $\delta_m = 3.5\text{‰}$ | |
| $F_{py} = 0.15 \times 10^{18} \text{ mol Myr}^{-1}$ | | |
| $F_{os} = 0.45 \times 10^{18} \text{ mol Myr}^{-1}$ | $\delta_{os} = -7\text{‰}$ | Aizenshtat et al. (2004) |
| $F_{\text{evap}} = 0.18 \times 10^{18} \text{ mol Myr}^{-1}$ | | |
| Scenario 2: $F_{os} = 3 \times F_{py}$; $F_v = 7.6 \times \text{modern}$ | | Hetzel et al. (2009); Adams et al. (2010) |
| $F_w = 0.21 \times 10^{18} \text{ mol Myr}^{-1}$ | $\delta_w = 6\text{‰}$ | |
| $F_v = 0.53 \times 10^{18} \text{ mol Myr}^{-1}$ | $\delta_v = 3\text{‰}$ | |
| $F_m = 0.04 \times 10^{18} \text{ mol Myr}^{-1}$ | $\delta_m = 3.5\text{‰}$ | |
| $F_{py} = 0.15 \times 10^{18} \text{ mol Myr}^{-1}$ | | |
| $F_{os} = 0.45 \times 10^{18} \text{ mol Myr}^{-1}$ | $\delta_{os} = -7\text{‰}$ | Aizenshtat et al. (2004) |
| $F_{\text{evap}} = 0.18 \times 10^{18} \text{ mol Myr}^{-1}$ | | |
| Scenario 3: $F_{os} = 6 \times F_{py}$; $F_w = 3.2 \times \text{modern}$; $F_v = 7.4 \times \text{modern}$ | | Blättler et al. (2011) |
| $F_w = 0.67 \times 10^{18} \text{ mol Myr}^{-1}$ | $\delta_w = 6\text{‰}$ | |
| $F_v = 0.52 \times 10^{18} \text{ mol Myr}^{-1}$ | $\delta_v = 3\text{‰}$ | |
| $F_m = 0.04 \times 10^{18} \text{ mol Myr}^{-1}$ | $\delta_m = 3.5\text{‰}$ | |
| $F_{py} = 0.15 \times 10^{18} \text{ mol Myr}^{-1}$ | | |
| $F_{os} = 0.90 \times 10^{18} \text{ mol Myr}^{-1}$ | $\delta_{os} = -7\text{‰}$ | Aizenshtat et al. (2004) |
| $F_{\text{evap}} = 0.18 \times 10^{18} \text{ mol Myr}^{-1}$ | | |

References

- Adams, D.D., Hurtgen, M.T. and Sageman, B.B. (2010) Volcanic triggering of a biogeochemical cascade during Oceanic Anoxic Event 2. *Nature Geosci.* 3, 201-204.
- Aizenshtat, Z. & Amrani, A. (2004) Significance of $\delta^{34}\text{S}$ and evaluation of its imprint on sedimentary organic matter: I. The role of reduced sulfur species in the diagenetic stage: A conceptual review. In: *Geochemical Investigations in Earth and Space Science: A tribute to Isaac R. Kaplan* (Eds. R.J. Hill, J. Leventhal, Z. Aizenshtat, M.J. Baedeker, G. Claypool), The Geochemical Society, Publication No. 9, 15-33.
- Blättler, C.L., Jenkyns, H.C., Reynard, L.M. & Henderson, G.M. (2011) Significant increases in global weathering during Oceanic Anoxic Events 1a and 2 indicated by calcium isotopes. *Earth Planet. Sci. Lett.* 309, 77-88.
- Brumsack, H.-J. (2006) The trace metal content of recent organic carbon-rich sediments: implications for Cretaceous black shale formation. *Palaeogeogr. Palaeoclimatol. Palaeoecol.* 232, 344-361.
- Burdett, J.W., Arthur, M.A. and Richardson, M.A. (1989) A Neogene sulphur isotope age curve from calcareous pelagic microfossils. *Earth Planet. Sci. Lett.* 94, 189-198.
- Canfield, D.E., Raiswell, R., Westrich, J.T., Reaves, C.M. and Berner, R.A. (1986) The use of chromium reduction in the analysis of reduced inorganic sulfur in sediments and shale. *Chem. Geol.* 54, 149-155.
- Clarkson, M.O., Poulton, S.W., Guilbaud, R., and Wood, R.A. (2014) Assessing the utility of Fe/Al and Fe speciation to record water column redox conditions in carbonate-rich sediments. *Chem. Geol.* 382, 111-122.
- Flögel, S., Wallmann, K., Poulsen, C. J., Zhou, J., Oschlies, A., Voigt, S. and Kuhnt, W. (2011) Simulating the biogeochemical effects of volcanic CO_2 degassing on the oxygen-state of the deep ocean during the Cenomanian/Turonian Anoxic Event (OAE2). *Earth Planet. Sci. Lett.* 305, 371-384.
- Fraústo da Silva, J.J.R. and Williams, J.J.P. (2001) *The Biological Chemistry of the Elements: The Inorganic Chemistry of Life*. Oxford University Press.
- Gill, B.C., Lyons, T.W. and Frank, T.D. (2008) Behavior of carbonate-associated sulphate during meteoric diagenesis and implications for the sulphur isotope proxy. *Geochim. Cosmochim. Acta* 72, 4699-4711.
- Goldberg, T., Shields, G.A. and Newton, R.J. (2011) Analytical constraints on the measurement of the sulfur isotopic composition and concentration of trace sulfate in phosphorites: Implications for sulfur isotope studies of carbonate and phosphate rocks. *Geostandards and Geoanalytical Research* 35, 161-174.
- Hansen, K.W. and Wallmann, K. (2003) Cretaceous and Cenozoic evolution of seawater composition, atmospheric O_2 and CO_2 : A model perspective. *Am. J. Sci.* 303, 94-148.

- Heinrichs, H., Brumsack, H.-J., Löffler, N. and König, N. (1986) Verbessertes Druckaufschlußsystem für biologische und anorganische Materialien. *Zur Pflanzenernährung und Bodenkunde* 149, 350-353.
- Hetzel, A., Böttcher, M.E., Wortmann, U.G. & Brumsack, H.-J. (2009) Paleo-redox conditions during OAE 2 reflected in Demerara Rise sediment geochemistry (ODP Leg 207). *Palaeogeogr. Palaeoclimatol. Palaeoecol.* 273, 302-328.
- Kiehl, J.T., Hack, J.J., Bonan, G.B., Boville, B.A., Williamson, D.L. and Rasch, P.J. (1998) The National Center for Atmospheric Research Community Climate Model: CCM3. *Journal of Climate* 11, 1131-1149.
- Kim, S.-J., Flato, G.M. and Boer, G.J. (2003) A coupled climate model simulation of the Last Glacial Maximum, part 2: approach to equilibrium. *Climate Dynamics* 20, 635–661.
- Kolonis, S. *et al.* (2005) Black shale deposition on the northwest African Shelf during the Cenomanian/Turonian oceanic anoxic event: Climate coupling and global organic carbon burial. *Paleoceanography* 20, PA1006, doi:10.1029/2003PA000950.
- Kolonis, S., Sinninghe Damsté, J.S., Böttcher, M.E., Kuypers, M.M.M., Kuhnt, W., Beckmann, B., Scheeder, G., and Wagner, T. (2002) Geochemical characterization of Cenomanian/Turonian black shales from the Tarfaya Basin (SW Morocco): relationships between paleoenvironmental conditions and early sulfurization of sedimentary organic matter: *Journal of Petroleum Geology* 25, 325-350.
- Kraal, P., Slomp, C.P., Forster, A., Kuypers, M.M.M. and Sluijs, A. (2009) Pyrite oxidation during sample storage determines phosphorus fractionation in carbonate-poor anoxic sediments. *Geochim. Cosmochim. Acta* 73, 3277-3290.
- Kuhnt, W. *et al.* (2001) Morocco basin's sedimentary record may provide correlations for Cretaceous paleoceanographic events worldwide. *EOS* 82, 361-364.
- Kuhnt, W., Luderer, F., Nederbragt, A., Thurow, J. and Wagner, T. (2005) Orbital-scale record of the late Cenomanian-Turonian Oceanic Anoxic Event (OAE-2) in the Tarfaya Basin (Morocco). *Int. J. Earth. Sci.* 94, 147-159.
- Kuypers, M.M.M., Pancost, R.D., Nijenhuis, I.A. and Sinninghe Damsté, J.S. (2002) Enhanced productivity led to increased organic carbon burial in the euxinic North Atlantic basin during the late Cenomanian oceanic anoxic event. *Paleoceanography* 17, PA1051, doi: 10.1029/2000PA000569.
- Leine, L. (1986) Geology of the Tarfaya oil shale deposit, Morocco: *Geologie en Mijnbouw*, 65, 57-74.
- Lüning, S., Kolonis, S., Belhadj, E.M., Belhadj, Z., Cota, L., Barić, G. and Wagner, T. (2004) Integrated depositional model for the Cenomanian-Turonian organic-rich strata in North Africa. *Earth Sci. Rev.*, 64, 51-117.
- Marotzke, J. (1991) Influence of convective adjustment on the stability of the thermohaline circulation. *J. Phys. Oceanogr.* 21, 903–907.

- März, C., Schnetger, B. and Brumsack, H.-J. (2010) Paleoenvironmental implications of Cenozoic sediments from the central Arctic Ocean (IODP Expedition 302) using inorganic geochemistry. *Paleoceanography* 25, PA320, doi:10.1029/2009PA001860.
- Meyers, S.R., Sageman, B.B. and Arthur, M.A. (2012) Obliquity forcing of organic matter accumulation during Oceanic Anoxic Event 2. *Paleoceanography* 27, PA3212, doi:10.1029/2012PA002286.
- Ohkouchi, N., Kawamura, K., Kajiwar, Y., Wada, E., Okada, M., Kanamatsu, T. and Taira, A. (1999) Sulfur isotope records around Livello Bonarelli (northern Appenines, Italy) black shale at the Cenomanian-Turonian boundary. *Geology* 27, 535-538.
- Paytan, A., Kastner, M., Campbell, D. & Thiemens, M.H. (2004) Seawater sulfur isotope fluctuations in the Cretaceous. *Science* 304, 1663-1665.
- Petit, G.R. and Van Tamelen, E.E. (1962) Raney Nickel desulphurization, In: Organic Reactions Vol. 12, John and Wiley & Sons, 356-380.
- Poulsen, C.J., Pollard, D. and White, T.S. (2007) General circulation model simulation of the ¹⁸O content of continental precipitation in the middle Cretaceous: a model-proxy comparison. *Geology* 35, 199–202.
- Poulton, S.W. and Canfield, D.E. (2005) Development of a sequential extraction procedure for iron: implications for iron partitioning in continentally derived particulates. *Chem. Geol.* 214, 209-221.
- Poulton, S.W. and Raiswell, R. (2005) Chemical and physical characteristics of iron oxides in riverine and glacial meltwater sediments. *Chem. Geol.* 218, 203-221.
- Rahmstorf, S. (1993) A fast and complete convection scheme for ocean models. *Ocean Modelling* 101, 9–11.
- Raiswell, R., Newton, R., Wignall, P.B. (2001) An indicator of water column anoxia: resolution of biofacies variations in the Kimmeridge Clay (Upper Jurassic, UK). *J. Sed. Res.* 71, 286-294.
- Redi, M.H. (1982) Oceanic isopycnal mixing by coordinate rotation. *J. Phys. Oceanogr.* 12, 1154–1158.
- Singer, A. (1980) The paleoclimatic interpretation of clay minerals in soils and weathering profiles. *Earth-Sci. Rev.* 15, 303-326.
- Sinninghe Damsté, J.S., Eglinton, T.I., Rijpstra, W.I.C., and de Leeuw, J.W. (1990) Characterization of sulphur rich high molecular weight substances by flash pyrolysis and Raney Nickel desulphurization. In: *Geochemistry of sulphur in Fossil Fuels* (eds. W.L. Orr and C.M. White). ACS Symposium Series American Chemical Society, Washington DC, p. 486-528.
- Strauss, H. (1999) Geological evolution from isotope proxy signals – sulphur. *Chem. Geol.* 161, 89-101.

- Thompson, S.L. and Pollard, D. (1997) Greenland and Antarctic mass balances for present and doubled atmospheric CO₂, from the GENESIS Version 2 Global Climate Model. *J. Climate* 10, 871–900.
- Voss, R. and Sausen, R. (1996) Techniques for asynchronous and periodically synchronous coupling of atmosphere and ocean models, part II: impact of variability. *Climate Dynamics* 12, 605–614.
- Wagner, T., Hofmann, P. and Flögel, S. (2013) Marine black shale deposition and Hadley Cell dynamics: A conceptual framework for the Cretaceous Atlantic Ocean. *Marine Petroleum Geology* 43, 222-238.
- Weaver, C.E. (1989) Clays, muds, and shales. *Developments in Sedimentology* 44, Elsevier, pp. 819.
- Wehausen, R. and Brumsack, H.-J. (2002) Astronomical forcing of the East Asian monsoon mirrored by the composition of Pliocene South China Sea sediments. *Earth Planet. Sci. Lett* 201, 621-636.
- Wignall, P.B. and Newton, R. (1998) Pyrite framboid diameter as a measure of oxygen deficiency in ancient mudrocks. *Am. J. Sci.* 298, 537-552.
- Zabel, M., Schneider, R.R., Wagner, T., Adegbe, A.T., De Vries, U. and Kolonic, S. (2001) Late Quaternary climate changes in Central Africa as inferred from terrigenous input to the Niger Fan. *Quat. Res.* 56, 207-217.
- Zegeye, A. et al. (2012) Green rust formation controls nutrient availability in a ferruginous water column. *Geology* 40, 599-602.
- Zhou, J., Poulsen, C.J., Pollard, D. and White, T.S. (2008) Simulation of modern and middle Cretaceous marine $\delta^{18}\text{O}$ with an ocean-atmosphere general circulation model, *Paleoceanography* 23, PA3223, doi:10.1029/2008PA001596.